Universidad del País Vasco Euskal Herriko Unibertsitatea
BILBOKO INGENIARITZA ESKOLA
ESCUELA DE INGENIERÍA DE BILBAO

MÁSTER UNIVERSITARIO EN

INGENIERÍA INDUSTRIAL

TRABAJO FIN DE MÁSTER

BAYESIAN OPTIMIZATION OF WIND FARM POWER GENERATION VIA WAKE STEERING USING ADM

Estudiante *Gonzalez Acha, Alvaro*
Directora *Herrero Villalibre, Saioa*
Departamento
Curso académico *2021-2022*

Bilbao, 5, sept, 2022

CRANFIELD UNIVERSITY

Alvaro Gonzalez Acha

BAYESIAN OPTIMIZATION OF WIND FARM POWER GENERATION VIA WAKE STEERING USING ACTUATOR DISK MODEL

SCHOOL OF WATER, ENERGY AND ENVIRONMENT
Renewable Energy MSc

MSc
Academic Year: 2021 - 2022

Supervisor: Dr Liang Yang
Associate Supervisor: Dr Patrick Verdin
September 2022

CRANFIELD UNIVERSITY

SCHOOL OF WATER, ENERGY AND ENVIRONMENT
Renewable Energy MSc

MSc

Academic Year 2021 - 2022

Alvaro Gonzalez Acha

BAYESIAN OPTIMIZATION OF WIND FARM POWER GENERATION VIA WAKE STEERING USING ACTUATOR DISK MODEL

Supervisor: Dr Liang Yang
Associate Supervisor: Dr Patrick Verdin
September 2022

This thesis is submitted in partial fulfilment of the requirements for the degree of Renewable Energy MSc

ABSTRACT

As new wind farms are built, the best locations are becoming fewer and fewer. Therefore, the debate is currently focused on possible measures to make better use of the resource. While the major reason for the drop in efficiency of a wind farm is wind speed variability, aerodynamic losses in large turbine arrays can be significant, potentially leading to a drop in annual energy production of up to 20%. There are several methods under study on how to improve the performance of wind farms, among which are the variation of yaw angle or axial-induction-based control, which is based on varying the pitch of the wind turbine blades or varying the torque.

This study provides a novel approach to the optimization of wake steering in wind farms via Bayesian Optimization. This way, if the upwind turbines are misaligned, their wakes may not directly affect the downstream turbines. Hence, increasing their power output and the output of the wind farm at the cost of lower power output in the upwind turbines. Therefore, this study chooses to develop a model to provide yaw angle variated optimizations.

The model to be used is based on the Actuator Disk Model and Large Eddy Simulations. To this end, a validation of the model used is first carried out by comparing the results obtained with those described in Jiménez et al. (2009). Once the code has been validated, a study of the possible optimisation of an array of turbines is carried out.

Keywords:

Velocity deficit, LES, viscosity, yaw angle.

ACKNOWLEDGEMENTS

Firstly, I would like to thank my supervisor, Dr Liang Yang, for his support, help and valuable advice throughout the individual project as well as Cranfield University and the Faculty of Engineering of Bilbao for giving me the possibility to participate in a project that has enriched me both personally and professionally and for providing me with the necessary computational resources for this project.

I would also like to thank all my friends who have supported me during these months to be able to face this challenge. Thanks to the Basques and Argentinians for making this experience in Cranfield unique and unrepeatable. To my flatmates for allowing me to acquire new knowledge and open up to new worlds. And, of course, thanks to my parents for allowing me to enjoy this experience.

TABLE OF CONTENTS

LIST OF FIGURES

LIST OF TABLES

LIST OF EQUATIONS

LIST OF ABBREVIATIONS

ADM	Actuator Disk Model
ALM	Actuator Line Model
BEM	Blade Element Momentum theory
CFD	Computational Fluid Dynamics

1 INTRODUCTION

To meet the targets, set in the Paris Climate Agreement (PCA), renewable energy production must increase to 67% of the global energy mix by 2050 [1]. This will help prevent global temperatures from rising by 1.5 - 2°C above pre-industrial levels [1], [2]. In this respect, it is necessary to develop low-cost and reliable energy production technologies.

One of the renewable technologies that best meets these conditions today is wind energy. In this sense, to comply with the PCA, wind farms must increase both in number and density of wind turbines. Likewise, as the locations with the best conditions for wind farms run out, it is necessary to access locations with less certain wind resources or more complex places for the implementation of the technology, such as offshore wind. That is why one of the main conundrums of wind technology is how to increase the efficiency of the remaining sites with lower wind loads.

While the major reason for the drop in efficiency of a wind farm is wind speed variability, aerodynamic losses in large turbine arrays can be significant (potentially leading to a drop in annual energy production of up to 20% [3]). In fact, in farms such as Horns Rev., depending on the wind direction the reduction of power with respect to the first row of turbines is found to be between 25-45% [3]–[5]. These aerodynamic losses occur due to the extraction of energy from the upwind turbines. This extraction from the atmospheric boundary layer causes a wake region immediately downstream of the rotor. In the case where the downwind turbine is not far enough downstream for the air to have recovered from the turbulence, the extraction of energy from the downwind turbine will be less than if unperturbed wind were to reach its rotor. Hence, the distribution of the wind farm is key in the study of the energy extraction of the farm. The distribution of the wind turbines within the wind farm is studied to try to produce an optimal power output, considering wind patterns in terms of directionality, speed, gusts... These studies typically result in the need for a larger streamwise spacing of turbines in the prevailing wind direction than in the other directions where the turbines may be closer together.

To minimise possible aerodynamic losses between wind turbines, the optimal streamwise spacing is 10-15D, where D is the diameter of the wind turbine [6]–[8]. However, due to land constraints or increased costs of transmission lines, among other factors, the distances are usually shorter (6-10D [9]). This may imply, in a worst-case scenario, a wind farm efficiency degradation of about 40% for wind directions aligned with the wind turbine columns in the farm [3]. Therefore, other strategies must be found to optimise energy extraction, like the optimization via wake steering.

If a turbine is misaligned with the incoming wind, there is a lateral forcing that deflects the wake region and therefore, if the upwind turbines are misaligned, the wake may not directly affect the downstream turbines [10]. Thus, increasing their power output and the output of the wind farm at the cost of lower power output in the upwind turbines. A small angle of misalignment can reduce the effect called partial wake overlap, which happens when a section of the wind turbine rotor area is in the wake of the upstream turbine while another section is in freestream conditions. This reduction also helps reduce fatigue from the wind turbine.

This paper aims to provide a novel wake steering control scheme via CFD simulations. It is not computationally feasible to explicitly model each rotor geometry of an entire wind farm. So, the influence of the rotor on the flow is represented by adding momentum source terms to the governing equations. There are several approaches to do so, the most common ones are ALM and ADM as will be detailed below.

The paper is structured as follows: section 2 and 3 presents the literature review and methodology followed, section 4 describes the numerical set-ups and results are provided in sections 5 and 6 alongside the conclusions in section 7.

2 LITERATURE REVIEW

In small wind farms or in the inflow region of large wind farms, the power output of the turbines for a fixed spacing strongly depends on the spacing combination in the chosen streamwise and spanwise directions. For such cases, the use of engineering wake models can be implemented. However, studies have shown that engineering wake models show difficulties in predicting wake effects in fully developed regimes, most likely due to the impossibility of reflecting the time-dependent interaction between different turbine wakes correctly [3], [8], [11].

These engineering models use simple linear equations, but more advanced models are available. Some of them are based on the parameterisation of the internal boundary layer growth combined with some eddy viscosity model like the ones shown in Refs. [8], [12]. On the other hand, other models estimate the wake of the wind turbine using linearised CFD models. An overview of the several wind turbine model approaches is presented in Sanderse et al. [13]. Moreover, different numerical modelling of wind turbine wakes using CFD studies are provided in Refs. [14]–[19]. Figure 2-1 represents the current most common methods used in literature.

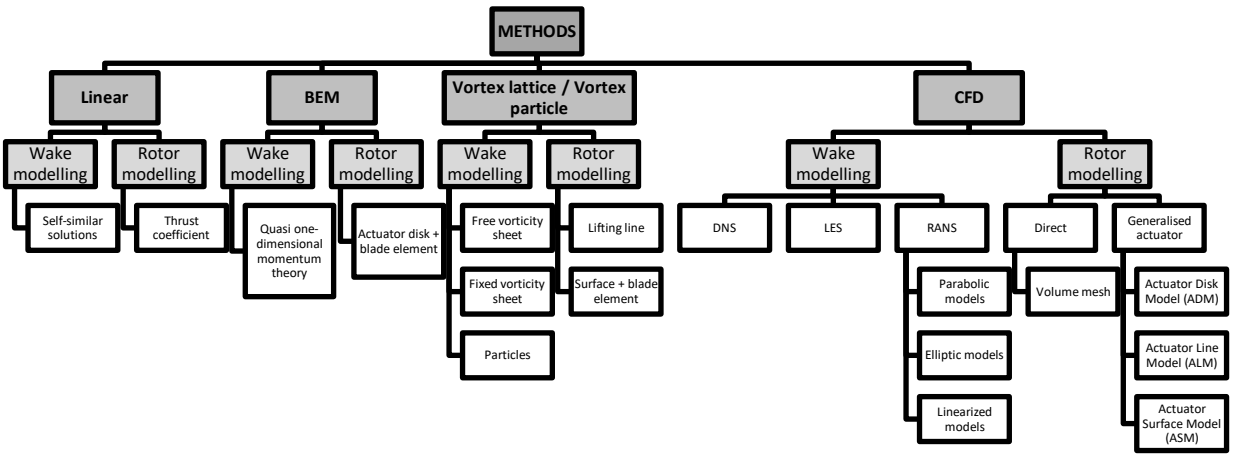

Figure 2-1. Classification of models [13].

To achieve reliable results on the wake effects of a wind turbine array, it is necessary to resort to high-fidelity computational simulations. The tool that uses

the fewest modelling assumptions is Direct Numerical Simulation (DNS). However, due to the scale disparity associated with flows with large numbers of Reynolds in the atmospheric boundary layer (ABL) and the near-blade boundary layer, DNS is not a tractable method for wind farm simulations. For this reason, a method of intermediate complexity between DNS and engineering models such as Large Eddy Simulations (LES) may be a suitable alternative for the prediction of wake interaction. LES, unlike DNS, is more tractable since the effect of smaller scales is accounted for by a subgrid-scale (SGS) model. Another solution could be to use Reynolds-averaged Navier-Stokes (RANS), but this approach is unable to predict turbulent vortex movements. This is not the case with the combination of LES and SGS models. Due to that capacity of resolving a large fraction of the turbulence, LES has become popular. Some studies using this model are presented in Refs. [14], [20]–[24].

To solve the LES equations in the near and far wake zones of the turbine, a representation of the turbine blades is needed. They can be represented in two ways: direct representation by discretising the actual blades in a computational mesh and generalised actuator disk approach (low order turbine models). The latter method consists of representing the blades by means of a body force (actuator disk, actuator line or actuator surface) and it is the method chosen for this report because it reduces computational costs and enables an easier mesh generation. The generalised actuator disk model introduces a force on the flow, generating momentum. Apart from that momentum, one should also introduce turbulence sources corresponding to the mechanical turbulence generated by the blades.

In the case of a uniformly loaded ADM, the force acting on the rotor (disk) surface is normally expressed as a function of the thrust coefficient. In the case of non-uniformly loaded disks, the force is dependent on the radial position. The sectional lift and drag coefficients are therefore used to obtain the local forces on the blades as in BEM.

In addition, apart from the axial loads (uniform or non-uniform), tangential forces are also introduced to consider possible rotational effects. Therefore, a distinction

can also be made here between ADM-R and ADM-NR (ADM with rotation and ADM with non-rotation respectively). A comparison between the two methods is shown in Porté-Agel et al. [25] and it is concluded that the inclusion of rotation and non-uniform loads improves the predictions of mean velocity and turbulence intensity with respect to the ADM-NR with uniform load. This effect is most evident in the centre of the wake, as the uniform strength model underestimates the turbulence intensity. Downstream, however, this effect is less noticeable. More simulations of ADM-NR are shown in Refs. [14], [26] using the traditional Smagorinsky model and Lagrangian scale-dependent dynamic model respectively. On the other hand, ADM-R simulations can be found in Refs. [25], [27], [28].

Another model also used is the ALM, which is basically an extension of the ADM with distributed loads. While the ADM wave vorticity model is a continuous sheet, the ALM can identify tip vortices. However, if 2D airfoil models are used, additional factors need to be known (Coriolis correction, centrifugal and tip effects) in addition to the lift and drag coefficients on the blades. A detailed comparison of the ADM-NR and ALM models using LES is shown in Stevens et al. [29]. From their conclusions, it is worth noting that since there is no rotation in the disk model, it does not represent the details of the flow (such as tip vortices) with as much resolution. However, in their study, they did not find a high-resolution wake regime where ALM has advantages over ADM, just more information about the radial distribution of the loads on the blades.

The methods mentioned so far can be used to study wake steering control which consists of the modification of the yaw angle, the angle between the rotor and the incoming wind. Wake steering has been shown to increase the total power output of a six-turbine array using LES [24] and using a two-turbine array experiment has also shown an overall increase in power output [30], [31]. Moreover, some studies consider the optimization under uncertainty (OUU) strategy to find yaw misalignments to maximize the energy extracted when there is any uncertainty in the yaw position [32]. Similarly, some studies use a similar OUU approach to find the optimal yaw offset considering the variability and uncertainty of the wind

direction for a fixed yaw position [33]. Besides, a study carried out by Kragh and Hansen [34] shows that wind turbine misalignment can also be used to reduce turbine loads, reducing fatigue by up to 20% in cases of light turbulence.

In a study carried out by Vollmer et al. [23], LES is used to study the behaviour of wake steering performance under variation in the ABL. The authors note that the wave shape under yawing conditions with respect to the inflow wind is curled rather than circular as many models predict. The curvature produced in this ripple affects the estimate of the centre of the wake. This ripple is produced by the counter-rotating vortices that appear in the flow behind the turbine and generate the distortion. This reasoning is consistent with the results of the experiments carried out in [35].

An alternative method to the yaw control could be the axial-induction-based control. This control method consists of the alteration of the blade pitch angle or the torque generation to reduce the axial induction factor of the upwind turbine to allow a higher velocity to reach downstream turbines. Several studies have been performed to investigate the effect of this control using wake models from engineering models [19], [36]–[38] to high-fidelity CFD models [19], [22], [39], [40]. However, not all studies conclude that this method has an actual beneficial effect on the performance of the wind farm. For instance, Bartl et al. [41] show how by pitching the blades of the upwind turbine the added kinetic energy in the wake cannot be leveraged by the downstream turbines since that energy is diffusing into the freestream. Recently, efforts are focused on dynamic induction control (DIC) since static induction control seem to provide poor power gains [19], [42]. Additionally, the combination of axial-induction-based control and yaw control is yet uncharted territory except for the experimental and numerical studies carried out by Park et al. [43], [44].

To carry out an optimization of the wake steering of a wind farm Bayesian Optimization (BO) can be used. BO is based on a Gaussian Process that tries to describe the function to be optimised. As the number of iterations increases, the posterior distribution of functions (Gaussian Process) improves. At each step a Gaussian Process is fitted to the previously explored points and the posterior

distribution together with an exploration strategy is used to determine the next point that should be explored [45], [46]. This exploration strategy can be Upper Confidence Bound (UCB) or Expected Improvement (EI) among others [47], [48]. The process is designed to minimise the number of steps needed to reach a combination of parameters that is close enough to the optimal combination. Therefore, this method tries to find the maximum of the acquisition function that incorporates exploration and exploitation, thus reducing computational expenses.

There are two problems when using BO in a physical system control. On the one hand, the difference between two successive inputs is often too large. On the other hand, the inputs are chosen from the region where the uncertainty is highest. In general, control actions cannot be changed so abruptly in a physical system and actions chosen from areas with high uncertainty can lead to significantly lower target values. BO has not been implemented in real-time control applications yet. This could be fixed by combining BO with gradient-free trust-region algorithms. In such a way the BO framework can be efficiently modelled for a small number of points. This method is called Bayesian Ascent (BA). In [46], BO is implemented, via BA, in a laboratory experiment to maximize the power production of a single wind turbine and the production of an array of two turbines. The control actions on the upstream turbine are changed gradually while the control actions on the downstream turbine are fixed. The results show that the BA algorithm can identify suboptimal upstream turbine conditions that increase the total energy extraction by adjusting the wake interaction.

3 METHOD

3.1 Governing equations

To calculate the flow field, the stabilised finite element method is used. The filtered incompressible Navier-Stokes equations can be written in a rotational form as the system of equations formed by (3-1) and (3-2).

$$\nabla \cdot u = 0 \tag{3-1}$$

$$\partial_t u - \nu \nabla^2 u + u \cdot \nabla u + \nabla p = f \tag{3-2}$$

Where u, p and ν represent the velocity field, pressure, and kinematic viscosity of the air respectively, and f is the added external body force per unit volume for modelling the effect of the wind turbine.

Both (3-1) and (3-2) are valued within a bounded domain of $\mathbb{R}^d$ denoted as Ω where d is the spatial dimension ($d = 2$ or 3) and in a time interval of $[0, T]$. This system of equations must be provided with the appropriate boundary and initial conditions. The boundary $\Gamma = \partial\Omega$ can be divided into the Dirichlet and Neumann boundaries (Γ_D and Γ_N respectively). Hence, the boundary and initial conditions are as follows in equations (3-3), (3-4) and (3-5).

$$u = \overline{u} \text{ on } \Gamma_D \times (0, T) \tag{3-3}$$

$$\left(-pI + \nu(\nabla u + (\nabla u)^T)\right) \cdot n = \overline{t} \text{ on } \Gamma_D \times (0, T) \tag{3-4}$$

$$u = u_0 \text{ in } \Omega \times \{0\} \tag{3-5}$$

Where n represents the unit normal vector to the surface Γ.

Furthermore, by adding a pseudo-derivative of the pressure, the artificial compressibility formulae can replace the divergence-free constraint. In this way, the system of equations formed by (3-1) and (3-2) is modified to the system formed by (3-2) and (3-6).

$$\partial_t p + \varepsilon^{-1} \cdot \nabla \cdot u = 0 \tag{3-6}$$

The artificial compressibility coefficient, ε^{-1}, may be used to evaluate an artificial speed of sound ($c = \sqrt{\varepsilon^{-1}}$). Thus, the higher this pressure-related speed, the closer (3-6) is to (3-1). This new formulation by adding artificial compressibility allows the use of an explicit time step model. However, the pressure-related speed will be a limiting factor of the explicit time step. The time step size used in this report verifies the following expression from equation (3-7).

$$\Delta t \leq \alpha \frac{\Delta h}{c} \tag{3-7}$$

Where α represents a factor dependent on the time integration scheme and Δh represents the minimum mesh size.

3.2 Low order turbine model

As previously mentioned, the turbines can be added through external body force terms acting on the flow. In the case of ADM-NR, the model chosen to represent the wind turbines is based on an empirical model for the calculation of the total thrust force experienced by the wind turbine. The thrust force per unit volume is modelled by the expression (3-8).

$$f_x^{disk} = \frac{1}{2} \cdot \frac{\rho}{\Delta_x} \cdot \bar{u}_0^2 \cdot C_T \tag{3-8}$$

Where C_T is the thrust coefficient, $\bar{u}_0$ is the upstream unperturbed streamwise velocity of the inlet flow in the centre of the rotor disk and $\Delta_x = L_x/N_x$ is the size of the grid in the streamwise direction (being L_x the streamwise domain length and N_x the number of grid points in that direction). Moreover, since the ADM-NR model considers a global thrust force for the entire rotor disk ignoring the rotation induced by the turbine, a constant thrust coefficient is assumed throughout the entire rotor disk.

$$C_T = \frac{T}{0.5 \cdot \rho \cdot \bar{u}_0^2 \cdot A_D} \tag{3-9}$$

Where T is the total thrust over the rotor area and A_D is the rotor disk area.

Nevertheless, in LES simulations for wind farms due to the high number of interactions between the wakes and the turbines, $\bar{u}_0$ is not really known for all turbines and arbitrary decisions are needed to determine the upstream distance to specify the speed [26]. One solution may be using the classical disk actuator theory which relates the velocity on the disk rotor, u_d and $\bar{u}_0$, through the induction factor (a).

$$u_d = (1 - a) \cdot \bar{u}_0 \quad \textbf{(3-10)}$$

To model thrust forces in the interaction of a fluid with the rotating blades, it will be necessary to use an average speed for the rotor disk over a period of time, obtaining a velocity denoted as $\langle \bar{u}_0^T \rangle_d$. Where T denotes time filtering and d denotes average over the rotor disk.

Thus, the total thrust force is presented in (3-11), where D is the diameter of the rotor disk and the local thrust coefficient is $C_T' = C_T/(1 - a)^2$.

$$F_T = \frac{\rho}{2} \cdot \langle \bar{u}_0^T \rangle_d^2 \cdot C_T' \cdot \frac{\pi}{4} D^2 \quad \textbf{(3-11)}$$

In the second approach, ADM-R, to take into account the turbine-induced rotational effect the forces are calculated following the BEM, where lift and drag coefficients can be obtained from tabulated data. This model considers N blade elements, and in each element, the lift and drag forces are perpendicular and parallel respectively to the direction of V_{rel}. The resulting force produces both thrust and rotational effects of the flow. Figure 3-1 shows the schematic of forces and velocities acting over a cross-sectional airfoil element at a radius r in the (x, θ) plane. The axial and tangential velocities are dependent on the position of the element and are denoted as $V_x = V_x(x, \theta)$ and $V_\theta = V_\theta(x, \theta)$ respectively. Moreover, the local relative velocity, V_{rel}, is defined as $V_{rel} = (V_x, \Omega r + V_\theta)$, where Ω represents the angular velocity of the blades. Hence, the axial and tangential forces are given by expressions (3-12) and (3-13).

$$F_x = \frac{1}{2} \cdot \rho \cdot V_{rel}^2 \cdot \frac{B}{2\pi r} \cdot c \cdot (C_L cos\varphi + C_D sin\varphi) \quad \textbf{(3-12)}$$

$$F_\theta = \frac{1}{2} \cdot \rho \cdot V_{rel}^2 \cdot \frac{B}{2\pi r} \cdot c \cdot (C_L sin\varphi - C_D cos\varphi) \quad \textbf{(3-13)}$$

Where B is the number of blades, c is the chord length, φ is the angle between V_{rel} and the rotor plane and C_L and C_D are the lift and drag coefficients respectively. Those two last coefficients are dependent on both the angle of attack ($\alpha = \varphi - \gamma$, being γ the pitch angle) and the Reynolds number based on V_{rel} and chord length, Re_c.

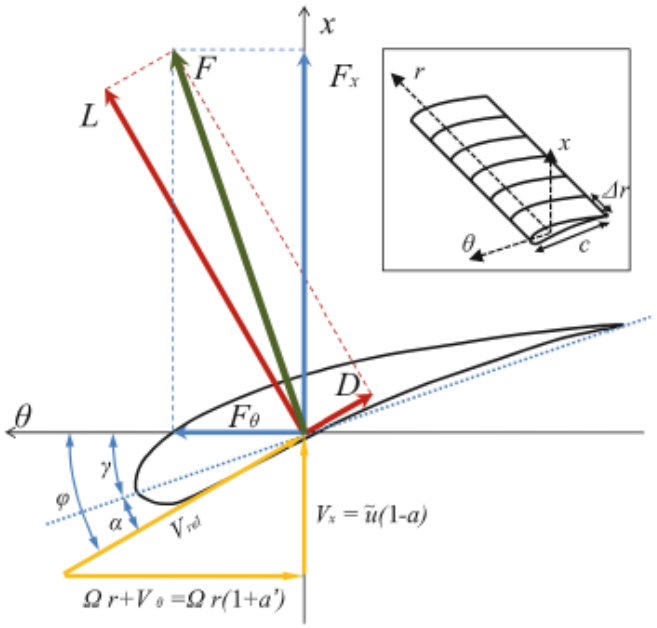

Figure 3-1. Force schematic of a cross-sectional airfoil element [27].

The resulting force per unit volume is given by expression (3-14).

$$f_x^{disk} = \frac{1}{2} \cdot \frac{\rho}{\Delta_x} \cdot V_{rel}^2 \cdot \frac{B}{2\pi r} \cdot c \cdot (C_L e_L + C_D e_D) \quad \textbf{(3-14)}$$

Where e_L and e_D represent the directions of the unit vectors for lift and drag respectively.

Furthermore, neither aeroelastic effects nor the effects of the tower shadow on blade aerodynamics are considered in this study. Not considering the aeroelastic effects imply that the blades act like rigid bodies and the presence of the tower may have a relative impact in terms of periodic variations of the loads over the blades.

Finally, these forces on the rotor are distributed in a three-dimensional Gaussian manner by the convolution of the force f and a regularisation kernel (η_ϵ).

$$f^\epsilon = f^{disk} \otimes \eta_\epsilon \quad \textbf{(3-15)}$$

Where the 2D and 3D regularisation kernels are defined by (3-16) and (3-17) being r_p the distance between the grid points and points on the actuator disk.

$$\eta_\epsilon{}^{2D} = \frac{1}{\epsilon^2 \pi} \exp\left[-\left(\frac{r_p}{\epsilon}\right)^2\right] \quad \textbf{(3-16)}$$

$$\eta_\epsilon{}^{3D} = \frac{1}{\epsilon^3 \pi^{3/2}} \exp\left[-\left(\frac{r_p}{\epsilon}\right)^2\right] \quad \textbf{(3-17)}$$

4 VALIDATION MODEL

The code must first be validated against previous models present in other studies and then used as a benchmark for the subsequent Bayesian optimization. The study chosen as a 2D validation model is carried out by Jiménez et al. [10], where the effect on the wake of a turbine is studied in the case of variations of the yaw angle. As in this study, Jiménez et al. characterize the turbulence generated by the presence of a wind turbine through a large eddy simulation with an ADM turbine and how it could affect downstream turbines.

As for the grid points, a mesh sensitivity analysis has been carried out. These settings differ from the setting used by [10], (256x96), since for the chosen air density it turns out to be an insufficiently accurate setting. Eight different mesh values have been used, ranging from the simplest mesh of [800x200] to the most complex of [3600x900]. All of them preserve the 4:1 ratio. As for the computational domain, a slightly larger domain will be used than the one detailed in the reference. Thus, the lengths in X and Y will be $L_x = 35D$ and $L_y = 8.75D$ as opposed to the $L_x = 34.9D$ and $L_y = 5.6D$ present in [10]. The diameter to be used is 60 m, and therefore the domain will have total dimensions of 2100x525 m. The reason for using a domain different from Jiménez et al. is based on two principles: on the one hand, to preserve the ratio of the grid points at 4:1 in the X and Y directions respectively; and on the other hand, to have a larger domain in the Y-direction and hence, to be able to study in greater detail the development in the diagonal direction of the domain in the cases of misalignment with the upfront wind.

The incident wind velocity is taken as in Jiménez et al. with a value of 6.3 m/s. Thus, considering the 60 m diameter, to achieve Reynolds numbers of the order of 10^2, viscosities of the order of 10^1 will be necessary. The value studied for the viscosity is 3 m^2/s, and therefore a Reynolds number of 252. Figure 4-1 shows a snapshot in time of the vortex structure of the wake due to the effect of the rotor disk for three different viscosities, in other words, different Reynolds numbers. For lower viscosity values (higher Reynolds numbers), it is observed that downstream of the rotor a series of vortices are produced that do not conform to

the reality of the wake that a wind turbine would generate from the point of view of 2D modelling. It is noticeable that the higher the number of Reynolds, the earlier the eddies are produced. But for the chosen viscosity, a homogeneous profile suitable for the object of study is observed.

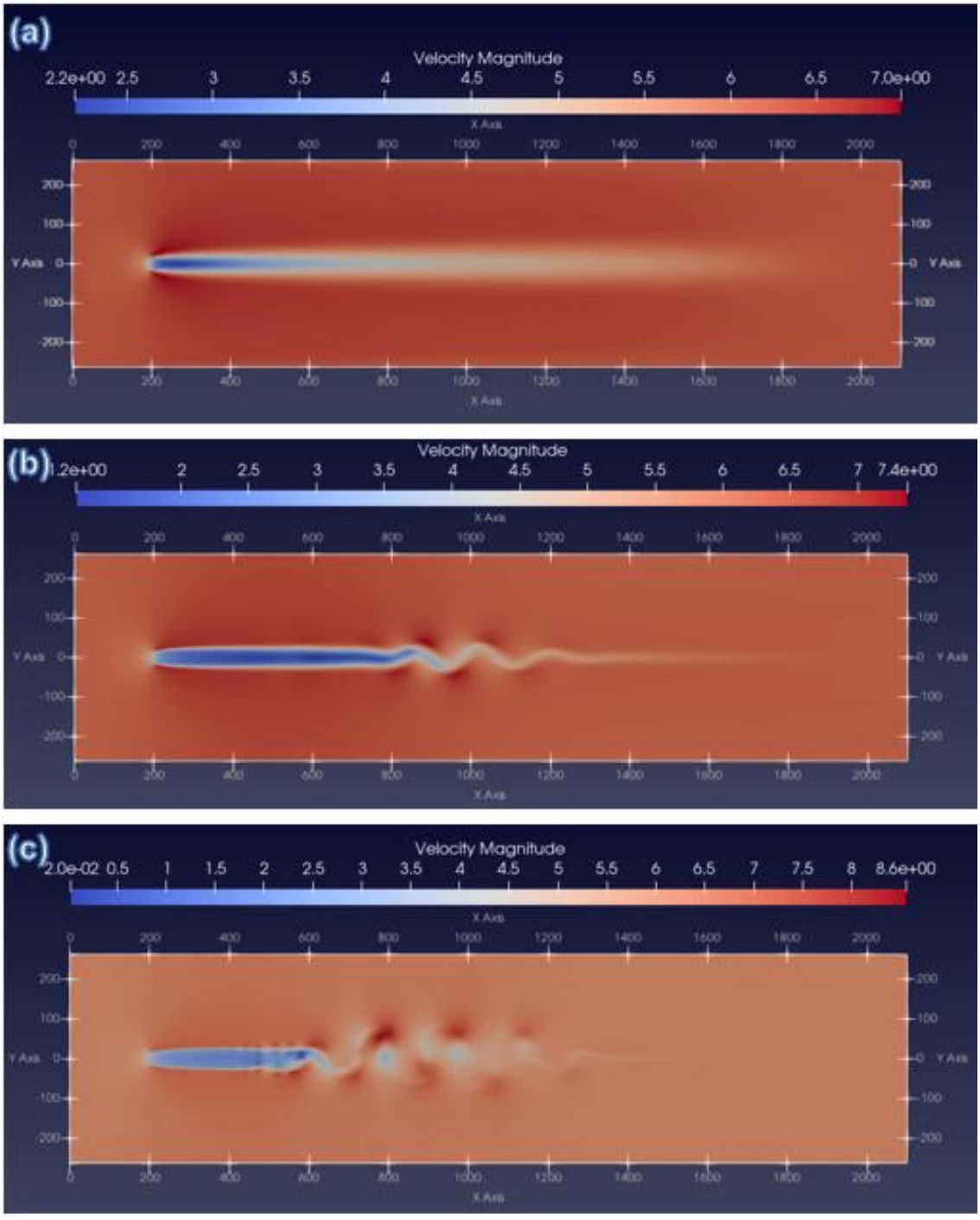

Figure 4-1. Instantaneous streamwise velocity field, $\boldsymbol{u_x}$, containing the rotor disk with a yaw angle of 0º, (a) Re = 252; (b) Re = 2,520; (c) Re = 25,200.

In addition, four boundary conditions are set in the domain, one for each boundary wall of the rectangle that forms the domain. For the wall where $(x, y) = (L_x, y)$, a boundary condition is established that assumes zero constant pressure on that wall. For the other three walls, i.e., for the cases $(x, y) = \left(x, L_y/2\right)$, $(x, y) = \left(x, -L_y/2\right)$ and $(x, y) = (0, y)$, a boundary condition is set that establishes a constant velocity equal to the freestream velocity.

The turbine rotor itself is modelled following the aforementioned ADM principles. In this way it is approximated by a group of rectangular cells in a Cartesian grid, thus being like a porous disk whose resolution will be composed of a total number of 160 cells. The centre of the turbine is placed at the point (200,0) of the domain as shown in Figure 4-1 and Figure 4-2.

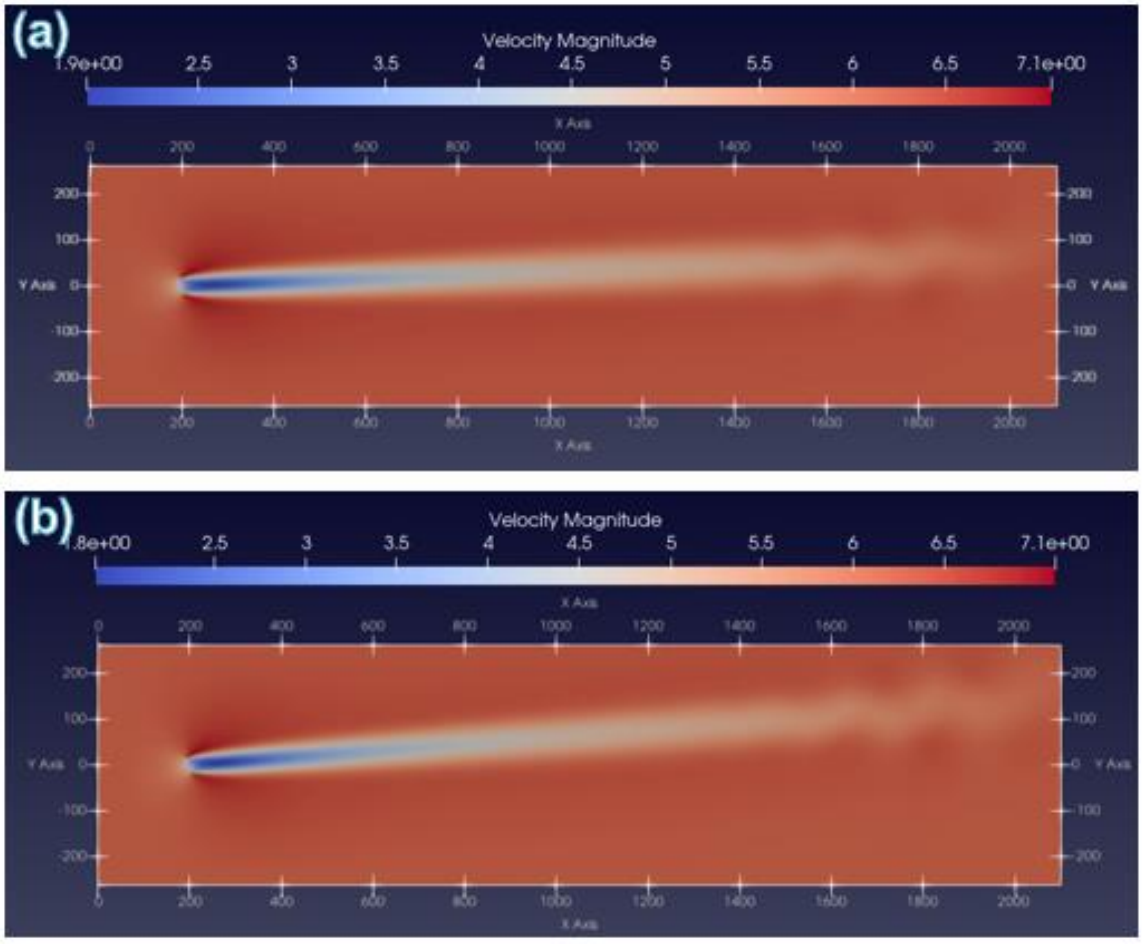

Figure 4-2. Instantaneous streamwise velocity field, $\boldsymbol{u_x}$, containing the rotor disk with a yaw angle of (a) 10º; (b) 20º.

The validation is performed at three levels downstream of the rotor, namely at distances $2.5D$, $5.5D$ and $8D$. So, since the position of the centre of the rotor disk is (200,0), those three levels are located at positions x = 350, 530 and 680 meters respectively. In this way, it is possible to observe the wake recovery, since the further the observer is from the turbine, the smaller the velocity deficit.

Moreover, for each of the above-mentioned distances, the effect of yaw misalignment is studied by means of three angles (0º, 10º and 20º). It can be considered that as the domain is symmetrical, the behaviour for the -10º and -20º angles will be identical to that portrayed by the 10º and 20º angles. This validates data from -20º to 20º, which will be the range chosen for the optimization phase. Figure 4-2 shows how the wake downstream of the rotor is modified due to the change of the yaw angle for angles of 10º and 20º. Considering Figure 4-1(a), a clear deviation can be observed that it can help to improve the extraction of energy from an aligned turbine wind farm.

4.1 Validation for a yaw angle of 0º

4.1.1 Mesh sensitivity analysis

To proceed with the validation, a sensitivity analysis is performed with the mesh grid sizes mentioned above. For this, the errors to be measured in the sensitivity analysis are considered to be the differences in absolute value of the minimum values achieved at distances of 2.5D, 5.5D and 8D. Ultimately, the reference values are as presented in Table 4-1 for the case of a yaw angle of 0°.

Table 4-1. Benchmark case for the 0º case with the minimum instantaneous velocity, $\boldsymbol{u_x}$, and the non-dimensional averaged streamwise velocity profile, $\boldsymbol{u_x/U_0}$, for the three downstream distances.

Parameter	Units	Min(2.5D)	Min(5.5D)	Min(8D)
u_x/U_0	-	0.51	0.76	0.85
u_x	m/s	3.21	4.77	5.34

If the viscosity value is set to 3 m^2/s, the other parameter for regulating the flow behind the rotor is the parameter *K_para*. This parameter states that the higher

the parameter, the higher the energy extraction by the rotor, and therefore the lower the downstream speed of the rotor.

It has been observed that as the precision of the mesh increases, for the same value of *K_para*, the errors become more noticeable. This is due to the fact that a higher accuracy allows a better knowledge of what happens downstream of the rotor and that for low accuracies the model establishes velocity deficits that do not adjust to reality. Thus, the bigger the precision, the bigger parameter of *K_para* will be required as presented in Table 4-2.

Table 4-2 compares different mesh grid sizes. The optimal values of *K_para* are presented, for which a minimum average error is achieved among the three distances analysed. It is also observed that the velocity profile that is most accurately approximated is the one related to the distance of 2.5D since it is the one that is most influenced by the variations of *K_para*. This can also be seen in Figure 4-3, how for the distances 5.5D and 8D a progressive reduction is achieved for each increase of the accuracy and the value relative to 2.5D the value is more stable hovering around lower values.

In Appendix A.1 a more comprehensive summary of the simulations is presented.

Table 4-2. Error breakdown for the three downstream distances and different mesh grid points with the respective optimized *K_para* parameter (yaw = 0º).

Mesh	**K_para**	**ε(2.5D)**	**ε(5.5D)**	**ε(8D)**	**ε_{avg}**
[800x200]	1.1	2.14%	11.29%	12.45%	8.63%
[1200x300]	1.7	0.51%	10.60%	11.28%	7.47%
[1600x400]	2.3	0.38%	9.38%	9.76%	6.51%
[2000x500]	3	0.53%	8.45%	8.39%	5.79%
[2400x600]	3.6	0.75%	6.71%	6.52%	4.66%
[2800x700]	4.4	0.12%	5.54%	4.94%	3.53%
[3200x800]	5.2	0.24%	4.07%	3.17%	0.24%
[3600x900]	6	0.84%	2.41%	1.29%	1.52%

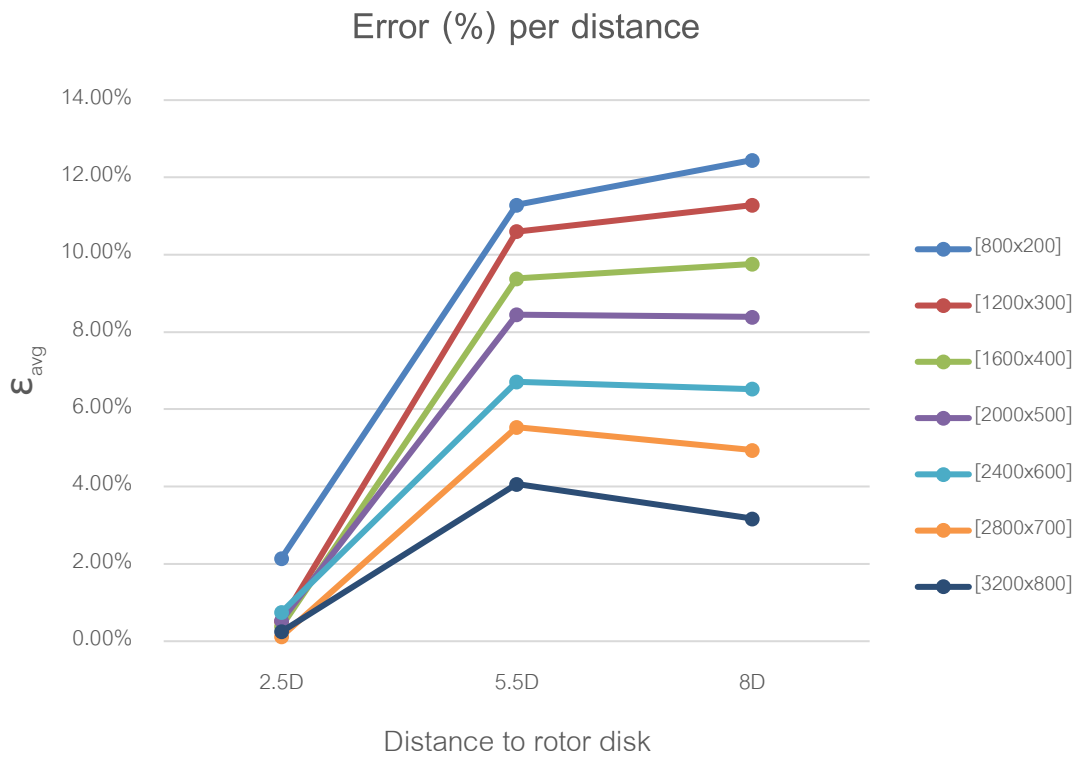

Figure 4-3. Error breakdown for the three downstream distances and different mesh grid points for the 0º case.

With the data presented in Table 4-2, it is, therefore, possible to carry out a study of mesh sensitivity. This study is presented in Figure 4-4, and as it can be concluded the slope is not steep enough to reach considerable reductions in the overall error up from 200,000 and 250,000 elements. Hence, from a mesh grid of approximately [3200x800] onwards, there is no clear benefit in terms of error reductions over validation considering the additional computational cost that such an error reduction would entail. Furthermore, it can be added that with around 150,000 elements the overall error is reduced to below 5%, which is a good enough value to consider the mesh [2400x600] valid compared to Jiménez et al.

However, it should be noted that in this sensitivity analysis for each different mesh, as mentioned above, the value of the parameter *K_para* that minimises the error made has been sought. In short, each mesh has a different value of *K_para* which implies that the analysis may not be a purely mesh sensitivity analysis by including the variance of *K_para*. If a single value of *K_para* were

used for all meshes, as can be inferred from the data in the table in Appendix A.1, the higher the mesh precision, the worse the overall error results.

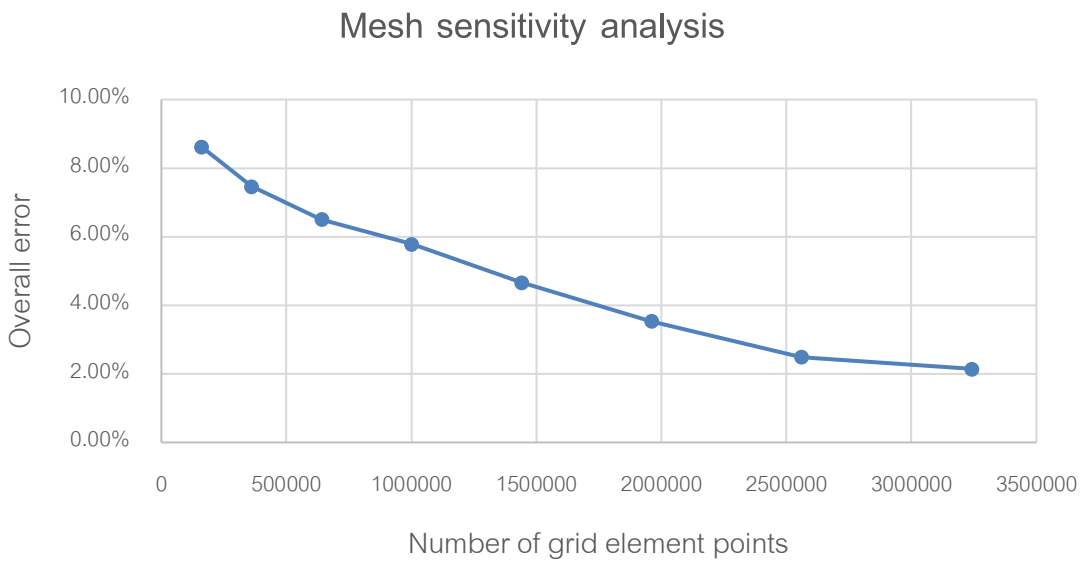

Figure 4-4. Mesh sensitivity analysis for a 2D case with a 0º yaw angle.

4.1.2 Velocity profiles

The velocity profile presented in Figure 4-5, corresponding to the 2.5D distance, shows that for this distance, regardless of the mesh chosen, good results are achieved, indeed, it is hardly possible to identify clear differences between them.

The most notable differences to the benchmark model are the values of the velocity profile for which it is not true that $-1 \leq y/D \leq 1$. These points correspond to the points in the domain which do not belong to the rotor disk, i.e., which are on its periphery. It is precisely at the points closest to the rotor disk that velocity spikes occur due to the interaction of the rotor disk with the circulating fluid. This can also be observed in the benchmark, but while in that case, the velocity spikes are close to 1%, for the model to be validated, spikes of over 5% are observed. However, these spikes do not represent a real threat to the validation of the model, since the object of study is the wake generated precisely in the area for which the condition of $-1 \leq y/D \leq 1$ is met.

The model also achieves a slimmer profile, where the speed deficit is more concentrated in the central area of the rotor disk and has a lower wind speed extraction capacity in the outer area of the disk.

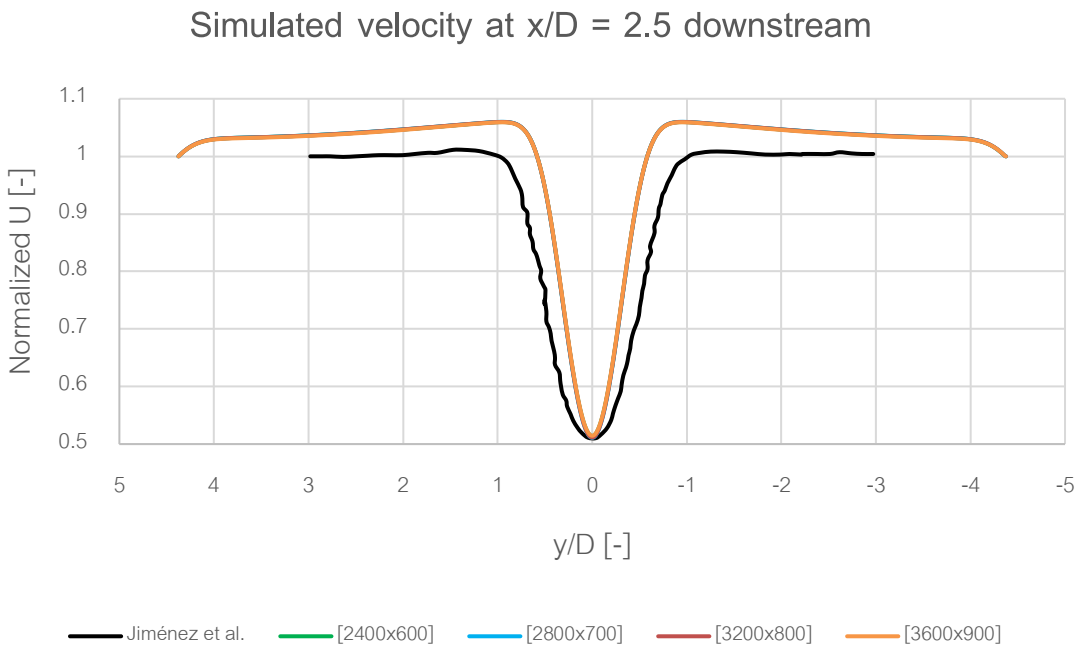

Figure 4-5. Non-dimensional averaged streamwise velocity profiles, $\boldsymbol{u_x/U_0}$, at 2.5D from turbine for yaw angle of 0º.

Figure 4-6, compared to Figure 4-5, shows a reduction in the speed deficit in the wake generated by the disk rotor. Thus, it drops from a reduction of about 50% to a reduction of about 30%. In contrast to the 2.5D case, for a distance of 5.5D, the same results are not achieved for all mesh sizes. It can be observed that as the accuracy increases, the speed deficit decreases and the benchmark values are reached with higher accuracy. Likewise, the previously described velocity spikes can also be observed, but they are logically less pronounced than in the situation closer to the rotor disk.

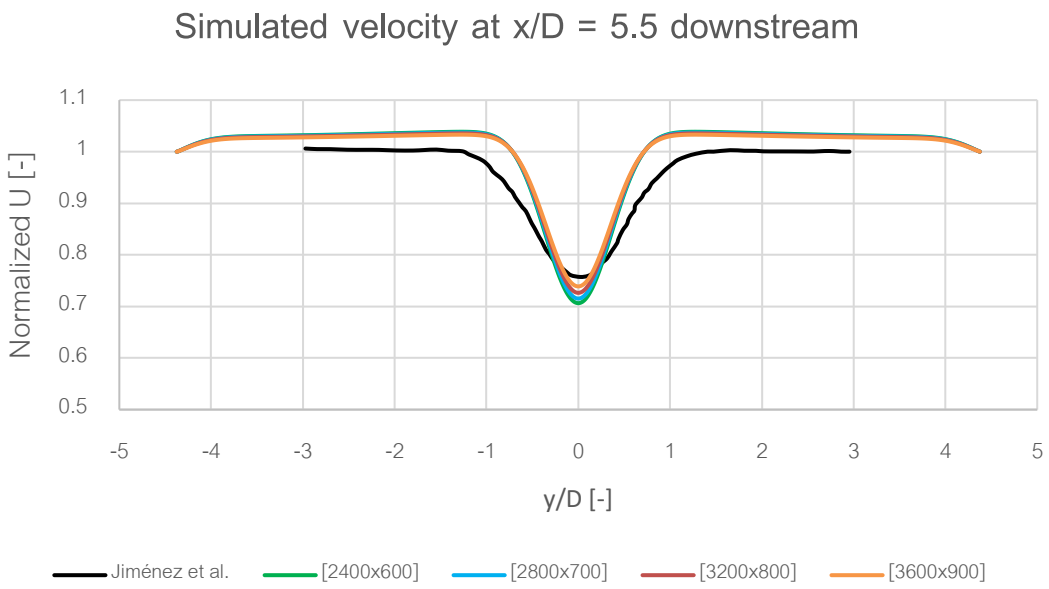

Figure 4-6. Non-dimensional averaged streamwise velocity profiles, $\boldsymbol{u_x/U_0}$, at 5.5D from turbine for yaw angle of 0º.

In the same way, as for the 5.5D case, the same things can be concluded for the 8D distance. First, an even smaller reduction is achieved, reaching 20%. Second, the higher the accuracy of the mesh, the closer the values are to the benchmark. And, thirdly, the speed spikes are even smaller than in the previous cases.

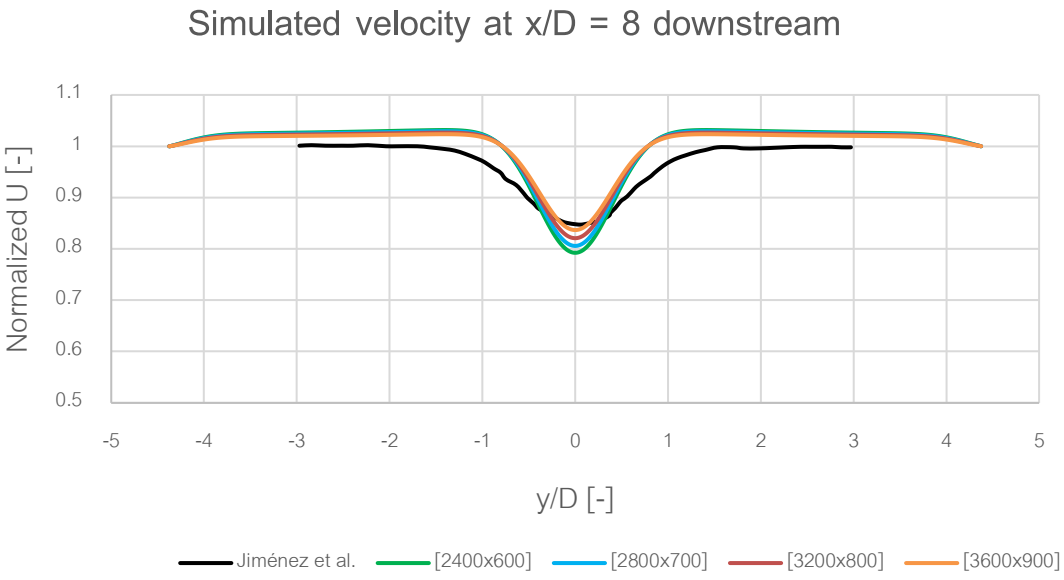

Figure 4-7. Non-dimensional averaged streamwise velocity profiles, $\boldsymbol{u_x/U_0}$, at 8D from turbine for yaw angle of 0º.

As a summary, Table 4-3 below shows the minimum values achieved by each distance analysed in comparison with the benchmark problem.

Table 4-3. Benchmark case for the 0º case with the minimum instantaneous velocity, $\boldsymbol{u_x}$, and the non-dimensional averaged streamwise velocity profile, $\boldsymbol{u_x/U_0}$, for the three downstream distances for the different meshes analysed.

Mesh	$\boldsymbol{u_x}$ **(2.5D) [m/s]**	$\boldsymbol{u_x}$ **(5.5D) [m/s]**	$\boldsymbol{u_x}$ **(8D) [m/s]**
Benchmark	3.21	4.77	5.34
[800x200]	3.28	4.23	4.68
[1200x300]	3.23	4.26	4.74
[1600x400]	3.23	4.32	4.82
[2000x500]	3.20	4.37	4.89
[2400x600]	3.24	4.45	4.99
[2800x700]	3.22	4.51	5.08
[3200x800]	3.22	4.58	5.17
[3600x900]	3.24	4.65	5.27

4.2 Validation for a yaw angle of 10º

4.2.1 Mesh sensitivity analysis

The reference values are as presented in Table 4-4 for the case of a yaw angle of 10°. If these values are compared with those given in Table 4-1, similar figures are observed. Surprisingly, for a given angle of yaw, there is a greater (albeit slight) reduction in speed, at least near the rotor. The major difference, of course, arises in the asymmetry shown in the velocity profile which will be discussed later.

Table 4-4. Benchmark case for the 10º case with the minimum instantaneous velocity, $\boldsymbol{u_x}$, and the non-dimensional averaged streamwise velocity profile, $\boldsymbol{u_x/U_0}$, for the three downstream distances.

Parameter	**Units**	**Min(2.5D)**	**Min(5.5D)**	**Min(8D)**
u_x/U_0	-	0.51	0.75	0.85
u_x	m/s	3.19	4.72	5.37

Due to time constraints, a study of 8 different mesh grids will not be carried out, but rather limited to four, from the simplest [800x200] to the most complex

[2000x500], that being 1,000,000 elements. So, if the dynamics of mesh sensitivity are similar to the case without yaw angle, its conclusions can be extrapolated.

In Table 4-5 the best simulation per mesh grid is presented and in Appendix A.2 a more comprehensive summary of the simulations is presented. According to the values in Table 4-5, it can be deduced that for a non-zero angle of rotation, lower errors are achieved. If we compare these values with those in Table 4-2, it can be appreciated that for the same mesh there is a lower overall error. Especially considering that for a mesh size of [1200x300], general errors of less than 5% are already achieved, which in the case of 0º yaw is not achieved until a mesh size of [2400x600]. However, it is also clear that higher values of *K_para* are necessary.

Table 4-5. Error breakdown for the three downstream distances and different mesh grid points with the respective optimized *K_para* parameter (yaw = 10º).

Mesh	**K_para**	**ε(2.5D)**	**ε(5.5D)**	**ε(8D)**	**ε_{avg}**
[800x200]	2.8	0.43%	9.41%	10.67%	6.83%
[1200x300]	4.2	2.66%	5.18%	5.97%	4.60%
[1600x400]	5.5	6.56%	0.28%	0.96%	2.60%
[2000x500]	7	1.66%	2.16%	1.35%	1.72%

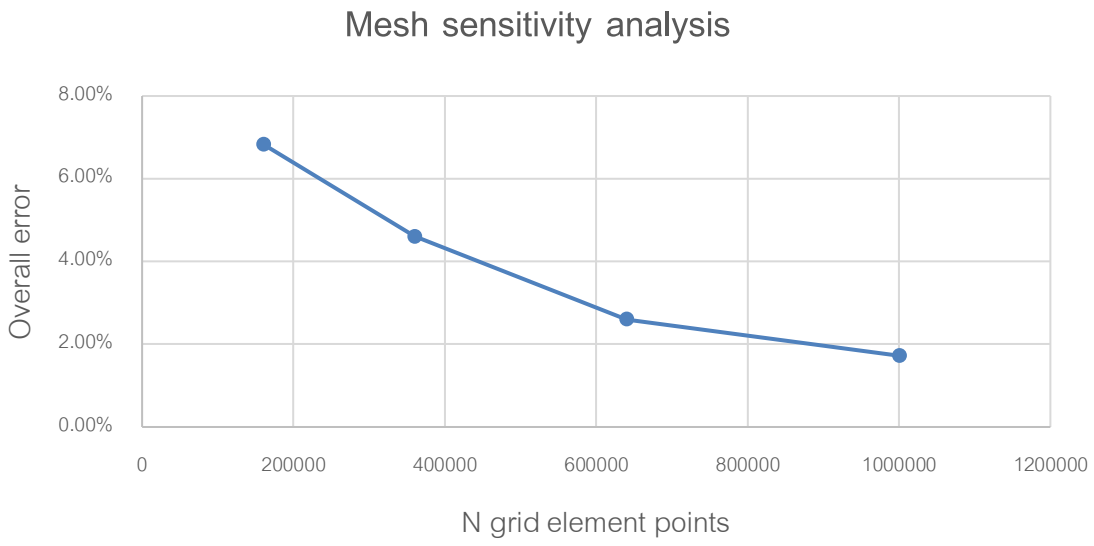

Figure 4-8. Mesh sensitivity analysis for a 2D case with a 10º yaw angle.

Furthermore, as in the case of yaw = 0º, the higher the mesh, the higher the error accuracy and although Figure 4-8 does not show a clear convergence of the error as in Figure 4-4, it can be assumed that increasing the mesh would lead to a similar conclusion.

4.2.2 Velocity profiles

As far as velocity profiles are concerned, the phenomenon of having a thinner profile in the disk rotor area ($-1 \leq y/D \leq 1$) continues to occur. However, it can be observed in Figure 4-9, Figure 4-10 and Figure 4-11 that there are no longer those speed excesses in the outer edges of the disk rotor that seemed so peculiar in the case of yaw = 0º. So, the velocity profiles of the model are more in line with the benchmark.

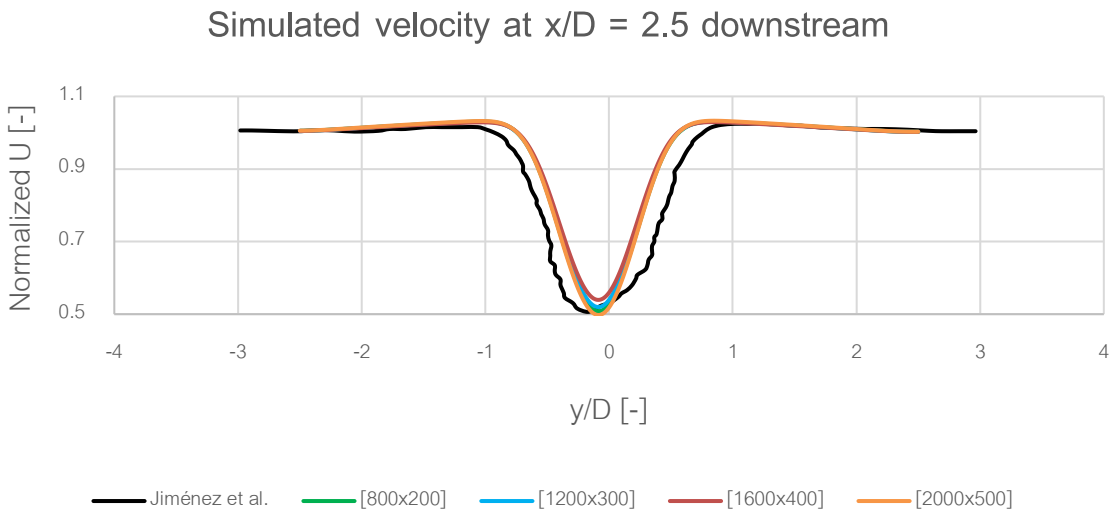

Figure 4-9. Non-dimensional averaged streamwise velocity profiles, $\boldsymbol{u_x/U_0}$, at 2.5D from turbine for yaw angle of 10º.

Figure 4-9 shows that for a small distance from the rotor there are hardly any deviations of the wake, thus maintaining a velocity profile symmetrical to the central axis. Moreover, as in Figure 4-5, for a distance of 2.5D, the velocity profile is practically identical regardless of the mesh.

In the case of Figure 4-10 and Figure 4-11, misalignment with the central axis is observed, so that the velocity profile becomes asymmetric. This misalignment is produced by the 10º angle of inclination of the rotor. For both profiles, a similar

misalignment is observed in terms of deviation with respect to y/D = 0. It can also be seen that for the simplest meshes, higher speed deficits are achieved, but as the mesh size increases, the closer to the benchmark value. Thus, reduction values of 25% and 15% are achieved for the 5.5D and 8D distances respectively.

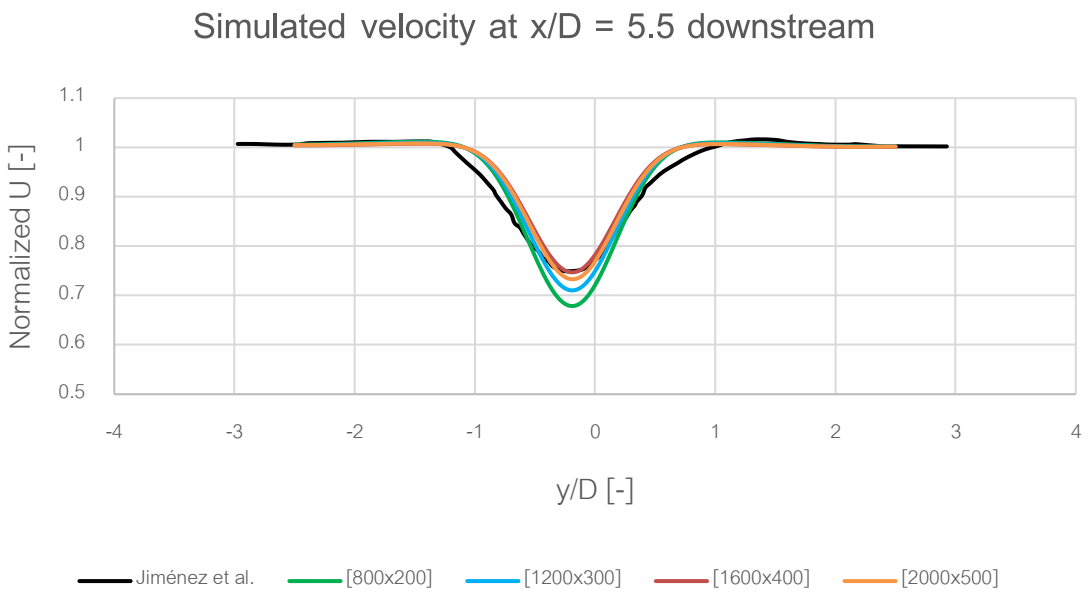

Figure 4-10. Non-dimensional averaged streamwise velocity profiles, $\boldsymbol{u_x/U_0}$, at 5.5D from turbine for yaw angle of 10º.

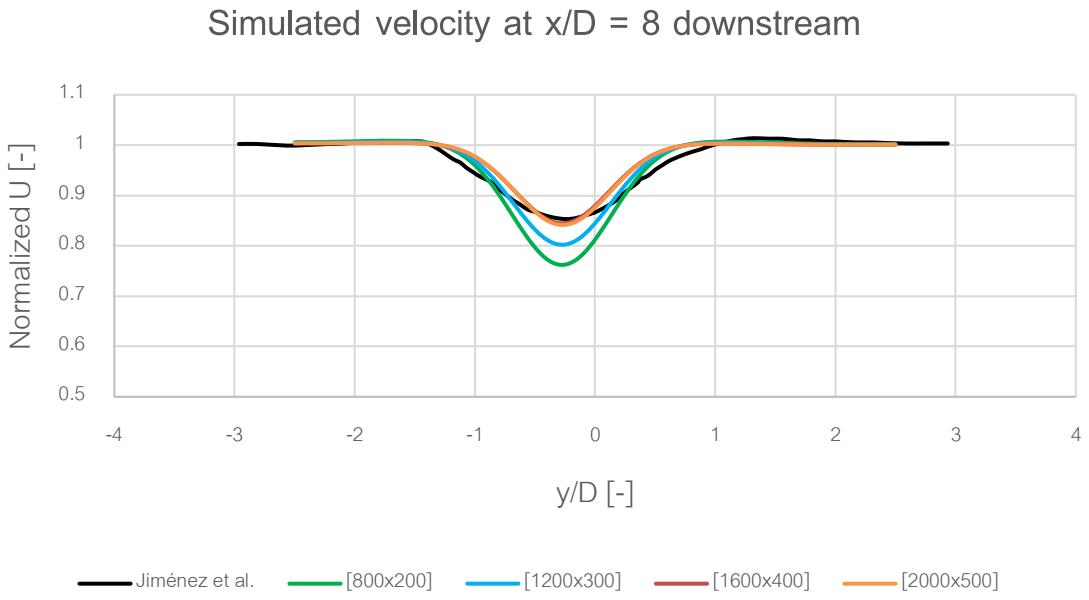

Figure 4-11. Non-dimensional averaged streamwise velocity profiles, $\boldsymbol{u_x/U_0}$, at 8D from turbine for yaw angle of 10º.

As a summary, Table 4-6 below shows the minimum values achieved by each distance analysed in comparison with the benchmark problem.

Table 4-6. Benchmark case for the 10º case with the minimum instantaneous velocity, $\boldsymbol{u_x}$, and the non-dimensional averaged streamwise velocity profile, $\boldsymbol{u_x/U_0}$, for the three downstream distances for the different meshes analysed.

Mesh	$\boldsymbol{u_x}$ **(2.5D) [m/s]**	$\boldsymbol{u_x}$ **(5.5D) [m/s]**	$\boldsymbol{u_x}$ **(8D) [m/s]**
Benchmark	3.19	4.72	5.37
[800x200]	3.20	4.28	4.80
[1200x300]	3.27	4.48	5.05
[1600x400]	3.40	4.71	5.32
[2000x500]	3.14	4.62	5.30

4.3 Validation for a yaw angle of 20º

4.3.1 Mesh sensitivity analysis

The reference values are as presented in Table 4-7 for the case of a yaw angle of 20°. Compared to the previous two cases, there is now a visible reduction in the amount of energy extracted by the wind turbine in terms of velocity deficit.

Table 4-7. Benchmark case for the 20º case with the minimum instantaneous velocity, $\boldsymbol{u_x}$, and the non-dimensional averaged streamwise velocity profile, $\boldsymbol{u_x/U_0}$, for the three downstream distances.

Parameter	**Units**	**Min(2.5D)**	**Min(5.5D)**	**Min(8D)**
u_x/U_0	-	0.56	0.77	0.86
u_x	m/s	3.56	4.84	5.42

As in the case of 10º, four different grids are studied. Similar to the previous cases, the best approximations for each of the chosen meshes are presented in Table 4-8 and the total breakdown is given in Appendix A.3. As can be seen in Figure 4-12 the trend of the error is similar to that of the 10º case, in other words, the higher the precision, the less error is achieved and convergence can be considered for higher magnitudes.

Interestingly, the values of *K_para* needed to achieve optimization for each mesh are lower than for the 10° case but higher than those needed for the 0° case. It

will be necessary for the optimization to reach some kind of compromise agreement to use a single value of *K_para* so that the validation performed is effective in the optimization.

Table 4-8. Error breakdown for the three downstream distances and different mesh grid points with the respective optimized *K_para* parameter (yaw = 20º).

Mesh	**K_para**	**ε(2.5D)**	**ε(5.5D)**	**ε(8D)**	**ε_{avg}**
[800x200]	2	1.04%	8.19%	10.37%	6.53%
[1200x300]	3	1.88%	5.99%	7.78%	5.21%
[1600x400]	4	2.97%	3.60%	5.04%	3.87%
[2000x500]	5.5	1.14%	2.09%	2.59%	1.94%

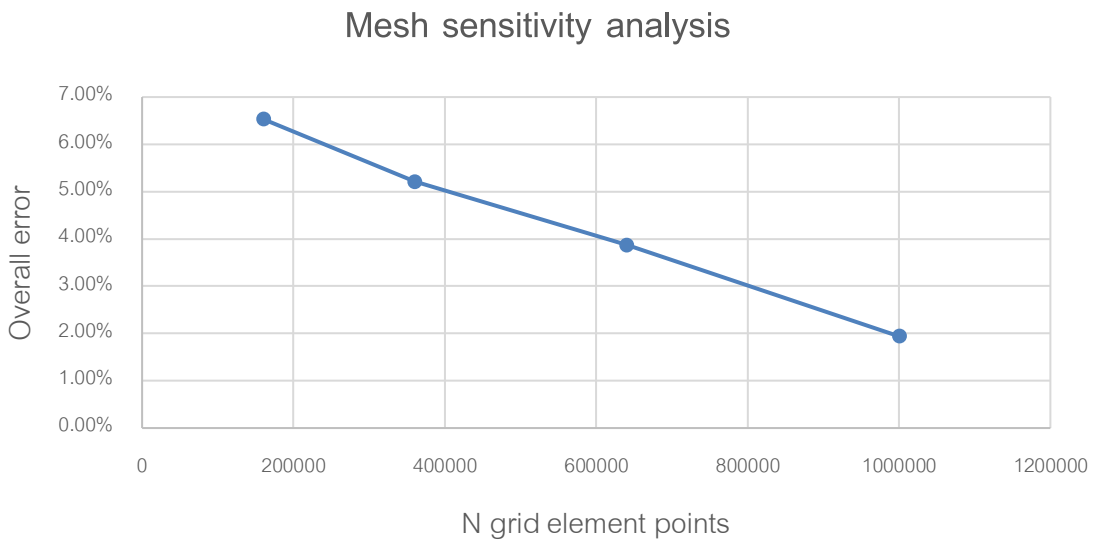

Figure 4-12. Mesh sensitivity analysis for a 2D case with a 20º yaw angle.

4.3.2 Velocity profiles

As expected, it is true that for a higher angle of rotation the speed deficits are reduced, i.e., the energy that the wind turbine is able to extract from the wind decreases. This phenomenon is observed in the aerodynamic profiles shown in Figure 4-13, Figure 4-14 and Figure 4-15. In Figure 4-13, it can be seen that for a distance of 2.5D, an increase in minimum downstream air speed of about 10% is achieved with respect to the case where the disk rotor is positioned perpendicular to the wind direction. Likewise, unlike the previous case where for

a distance of 2.5D a misalignment with respect to the central axis was not observed, in the case of 20º, this phenomenon is observed. In fact, in the three figures, this misalignment is more noticeable than in the 10º case, logically due to the 10º increase in this case.

As has already happened in the other cases, for a distance of 2.5D there are hardly any differences between the different meshes and the profiles are thinner than the benchmark. In addition, Figure 4-14 and Figure 4-15 show that the larger the mesh size, the higher the accuracy and the lower the speed deficit. In these two figures, it can also be seen how the profile walls are more in line with the benchmark without being as thin as in the case of 2.5D. However, it can also be noticed how for positive values ($(0 \leq y/D \leq 1)$ it moves further away from the benchmark due to the interaction between the upper corner that interacts with the wind, this corner of the rotor is the one that suffers the most in this position due to that peek speed.

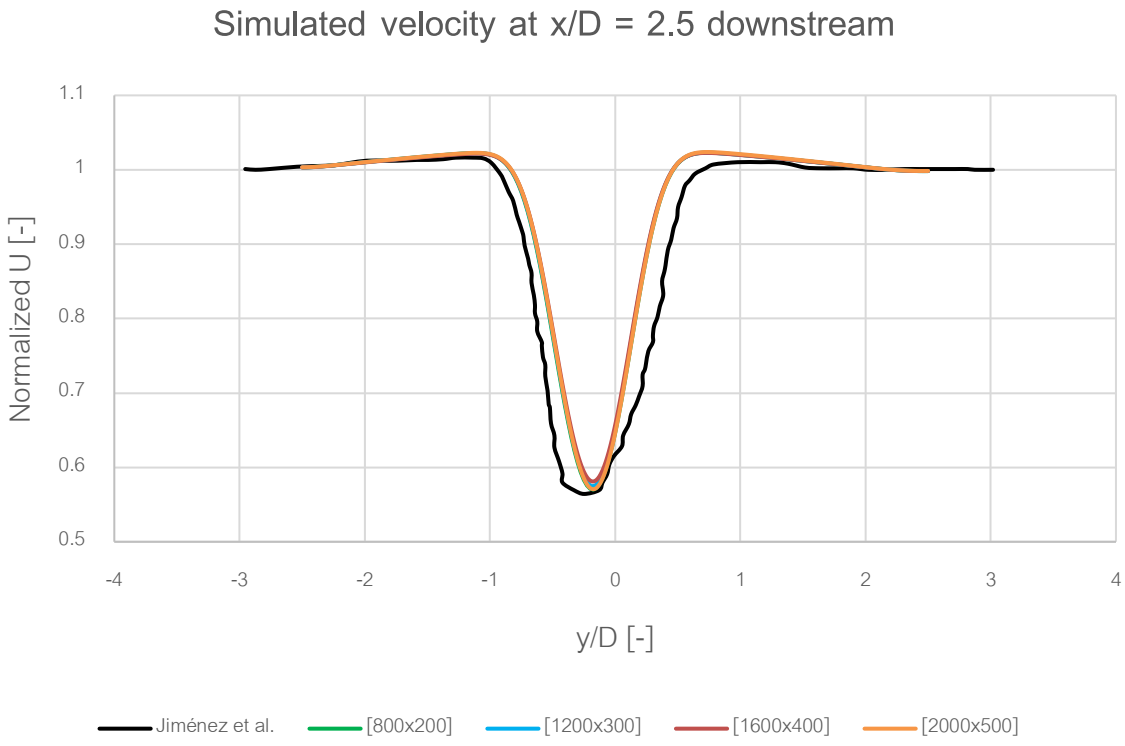

Figure 4-13. Non-dimensional averaged streamwise velocity profiles, $\boldsymbol{u_x/U_0}$, at 2.5D from turbine for yaw angle of 20º.

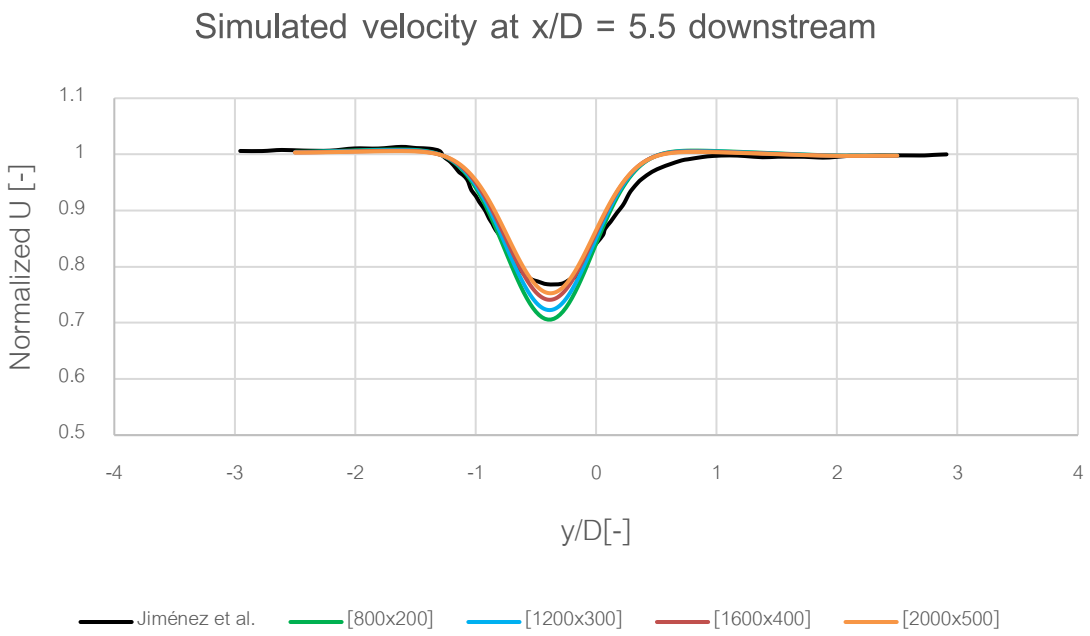

Figure 4-14. Non-dimensional averaged streamwise velocity profiles, $\boldsymbol{u_x/U_0}$, at 5.5D from turbine for yaw angle of 20º.

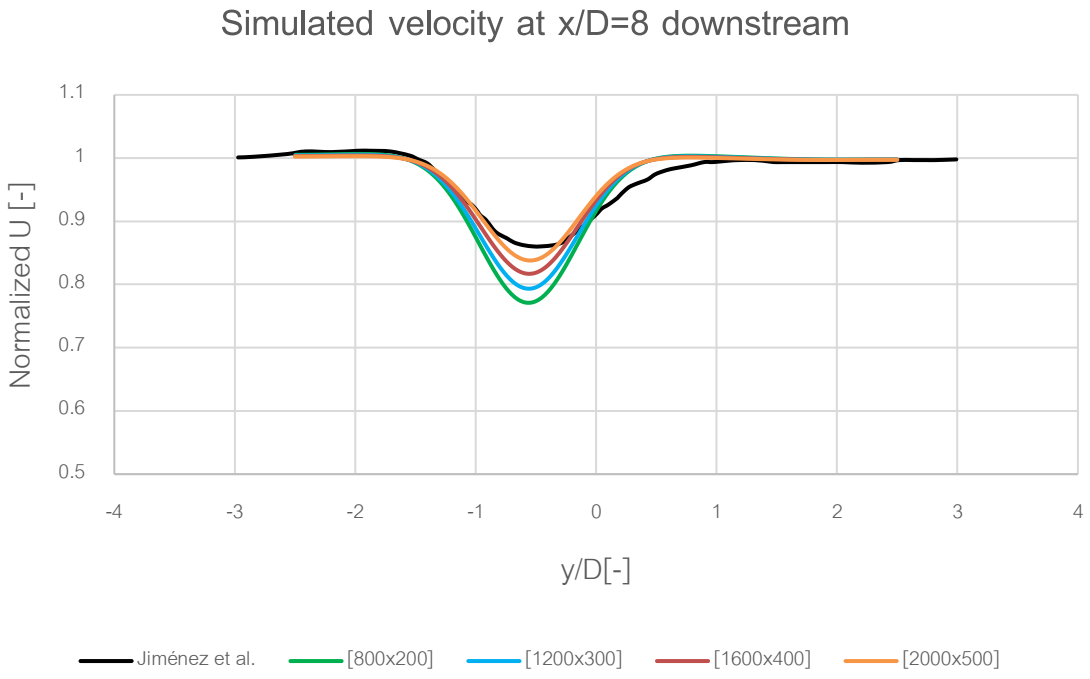

Figure 4-15. Non-dimensional averaged streamwise velocity profiles, $\boldsymbol{u_x/U_0}$, at 8D from turbine for yaw angle of 20º.

As a summary, Table 4-9 below shows the minimum values achieved by each distance analysed in comparison with the benchmark problem.

Table 4-9. Benchmark case for the 20º case with the minimum instantaneous velocity, u_x, and the non-dimensional averaged streamwise velocity profile, u_x/U_0, for the three downstream distances for the different meshes analysed.

Mesh	u_x **(2.5D) [m/s]**	u_x **(5.5D) [m/s]**	u_x **(8D) [m/s]**
Benchmark	3.56	4.84	5.42
[800x200]	3.59	4.45	4.86
[1200x300]	3.62	4.55	5.00
[1600x400]	3.66	4.67	5.15
[2000x500]	3.60	4.74	5.28

5 MODEL'S VELOCITY PROFILES

Before starting with the description of the Bayesian optimization, the velocity profiles for different yaw angles discussed earlier in section 4 are presented in Figure 5-1, Figure 5-2 and Figure 5-3 below. Taking into account that for the 0º case there is a wider range of meshes up to [3600x900] while for the 10º and 20º cases it only goes up to [2000x500], it is decided to use the results for this mesh that all the cases have and which is more precise, i.e. [2000x500], as a comparative method.

In the three figures it can be noticed different characteristics mentioned above. Firstly, as the yaw angle increases, the minimum value of the profile moves away from the centre of the axis and it is no longer symmetrical with respect to the y/D axis. Secondly, this increase in yaw also implies that the loss of wind speed decreases, which does not occur for the particular case in which the yaw angle is 10º and the distance to the rotor is 2.5D, but it does for the rest of the cases.

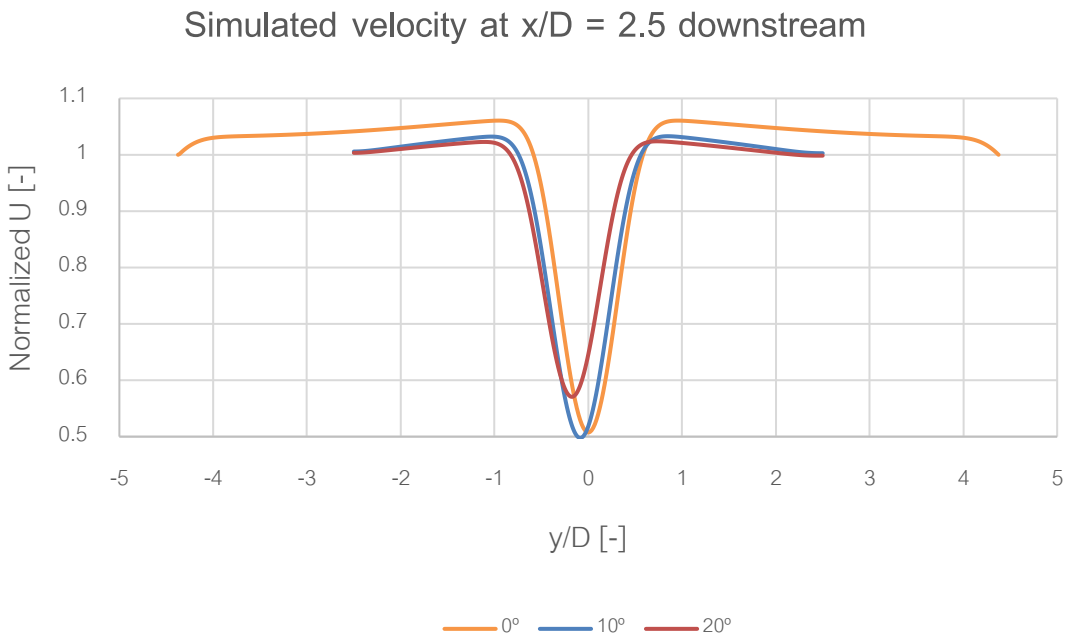

Figure 5-1. Non-dimensional averaged streamwise velocity profiles, $\boldsymbol{u_x/U_0}$, at 2.5D from turbine for different yaw angles.

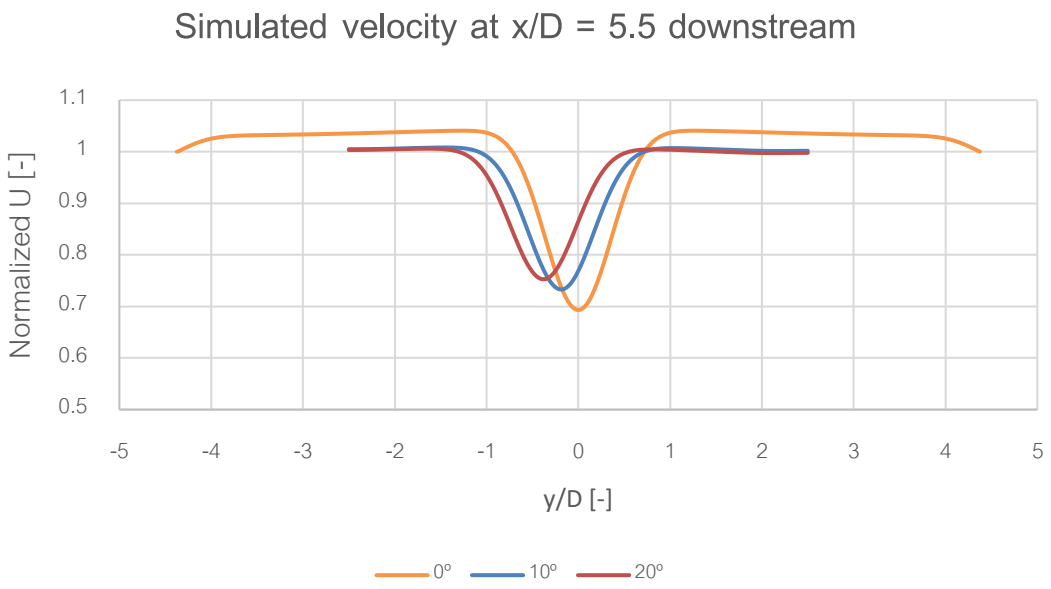

Figure 5-2. Non-dimensional averaged streamwise velocity profiles, $\boldsymbol{u_x/U_0}$, at 5.5D from turbine for different yaw angles.

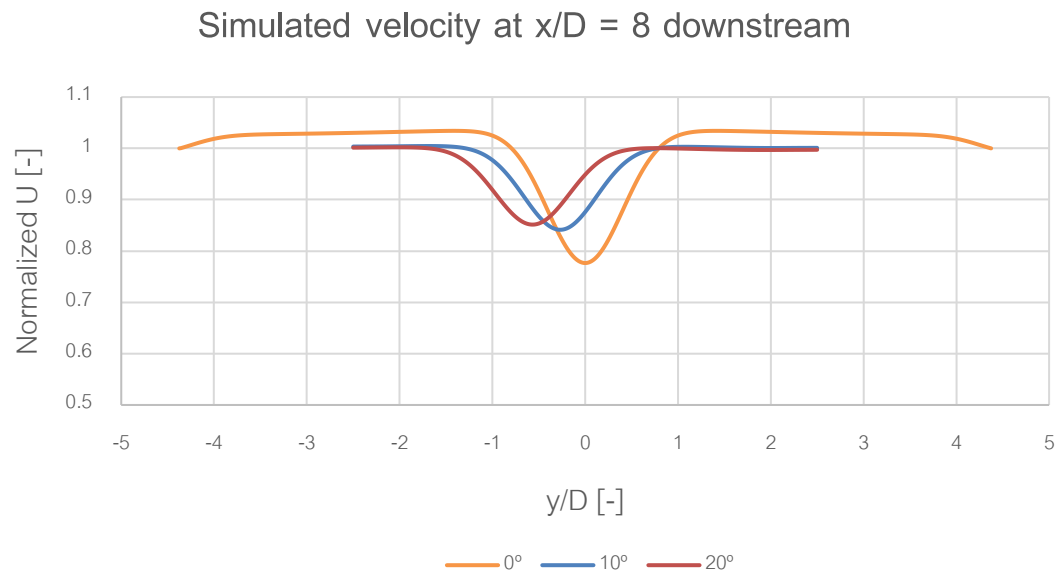

Figure 5-3. Non-dimensional averaged streamwise velocity profiles, $\boldsymbol{u_x/U_0}$, at 8D from turbine for different yaw angles.

Furthermore, having used different values of *K_para* for the different cases, a compromise must now be reached to establish a single value of *K_para* so that the optimization fits as closely as possible to the possible validation case. Besides, it will only be done for the four cases that the three angles have tested.

In this way, the following has been proposed, as shown in Table 5-1. It can be seen that by averaging the values obtained, a linear upward trend is obtained as the mesh size increases.

Table 5-1. *K_para* parameter for the different angle cases.

Mesh	**K_para (0º)**	**K_para (10º)**	**K_para (20º)**	**K_para (opt)**
[800x200]	1.1	2.8	2	1.9
[1200x300]	1.7	4.2	3	2.9
[1600x400]	2.3	5.5	4	3.9
[2000x500]	3	7	5.5	5.1

6 BAYESIAN OPTIMIZATION

The study of the possible optimization will be carried out using an array of two turbines aligned with respect to the incident air flow. The first turbine is located at the same point as for the validation case, i.e., the centre of the disk rotor is at position (200,0). Taking into account the usual distances in onshore wind farms, the second turbine is placed at a distance downstream in the dominant wind direction of 7D, that is, at position (620,0). Logically, both turbines start from a similar position: both have the same diameter and at the beginning of the optimization both have a zero-yaw angle.

For the sake of saving computational time, the total domain is reduced from the value used in the validation of total dimensions of 2100x525 m to 1200x300 m. Thus, it is possible to reduce the total size to be studied while preserving the size ratios to have square grid cells with the ratio of 4:1 in the X and Y directions respectively.

The Bayesian optimization process consists of an iterative process of randomising scenarios in which the best possible combination of factors studied is extracted. In other words, for each test that is carried out, a certain number of possible scenarios are randomly established and the best of these scenarios is extracted. In this way, the greater the number of scenarios, the greater the precision of the final optimised result. Thus, a possible optimization is first studied in the case in which the yaw angle rotates from an angle of -20º to an angle of 20º for the upwind turbine, while the angle of the downstream turbine is kept constant at 0º. Subsequently, a study is carried out to see if a better optimization is achieved in the case where the downstream turbine also rotates from the angle -20º to 20º.

When choosing the best scenario within each test, the best scenario is chosen based on the total average power generated by the two turbines. It should be noted that depending on the value of *K_para*, taking into account that it is a parameter that regulates the amount of fluid through the disk rotor and therefore regulates the power extraction, different power values are obtained. In short, for

each mesh, having used different values of *K_para*, different average power values are obtained. And, therefore, the power results should not be compared between different meshes, but the comparison should be made between the different yaw angles obtained in the different optimization tests. It should also be noted that by using a different viscosity than the real one (3 m^2/s versus $1.5 \cdot 10^{-5}$ m^2/s), the average power values are different from what would be obtained in a real wind farm.

Figure 6-1 shows an example of the case described so far, with two turbines aligned and the first one at a certain angle to the incident wind. It can be seen that due to the wake generated by the upwind turbine, the wake generated by the second turbine has lower speeds. That is to say, as the second turbine receives a wind with a lower speed, this turbine produces a wind with an even lower speed. Each of the iterations is lengthened sufficiently to allow the downstream flow to be fully developed by the time it reaches the second turbine so that the effect of the upwind turbine on the second turbine can be studied.

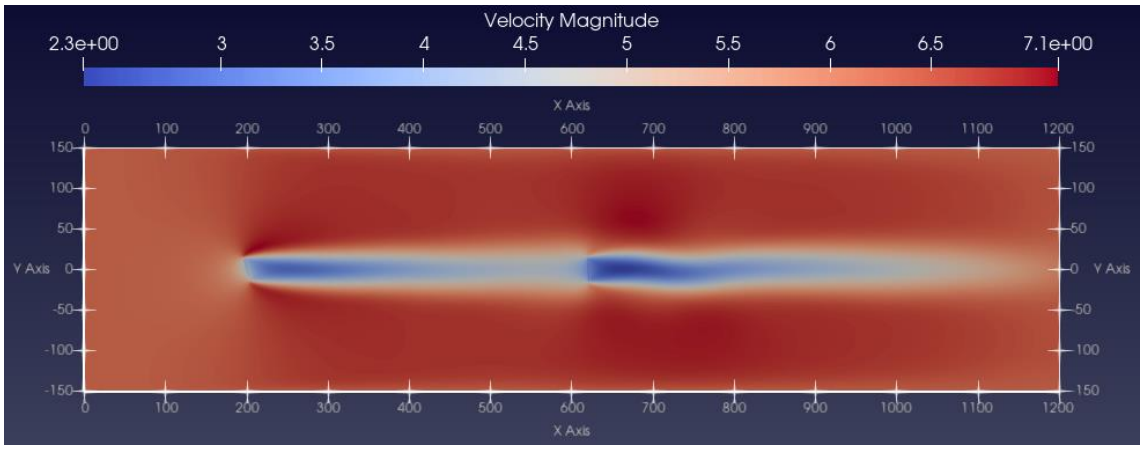

Figure 6-1. Instantaneous streamwise velocity field, $\boldsymbol{u_x}$, containing the two-array turbine for different yaw angles between turbines.

6.1 First mesh approach

For the first mesh of [800x200], 3 tests have been carried out, resulting in 30 different possible cases. From these, the best of each mesh is selected and therefore there are three possible yaw angles, which are detailed in Table 6-1. The average power produced for each of these angles is also shown.

Table 6-1. Optimization results for a mesh of [800x200].

Test	Average Power Output (W)	Yaw angle
1	134,947.16	-5.78º
2	133,438.67	5.74º
3	134,300.38	-8.13º

Surprisingly, two of the three simulations that have been carried out for this mesh achieve a very similar misalignment angle between them. One for a negative yaw angle and another for a positive yaw angle but considering that the second turbine is maintained with a zero-yaw angle, the system is symmetrical and for these cases the yaw angle's sign is irrelevant. For the three cases, practically the same average power output is obtained and if the breakdown of Appendix A.4 is observed, it can be seen that the variations of the power output for the 30 cases barely vary by 5% between the highest value obtained and the lowest. The logical conclusion from these three tests is that for all three, an upstream turbine rotation angle is required to generate a higher total power output from the two-turbine array. In addition, it is observed that the yaw angle can be increased to a certain point beyond which lower power is achieved. In this case, it is observed that for an angle of 5.74º there is still room for improvement but that for an angle of 8.13º this maximum has already been reached and power is no longer being gained.

Figure 6-2 shows two aerodynamic profiles relative to the best case achieved in these 30 scenarios. The first profile shows the velocity profiles of the turbines and the effect of the first turbine on the second turbine is palpable. It should also be added that with a yaw angle of 5.78º, an improvement in the air reaching the second turbine is achieved. The second profile shown in Figure 6-2 is the pressure profile not shown in the whole document so far. It can be noticed that due to the effect of the wind turbine, as in practice, depressions are achieved downstream of the rotor and consequently overpressures are achieved just before the air interacts with the rotor disk. This effect is suffered to a greater extent by the upwind turbine for two reasons: on the one hand, as it works at higher speeds, the pressure gradient is more noticeable, and on the other hand,

is turned with respect to the incident wind which accentuates this overpressure effect.

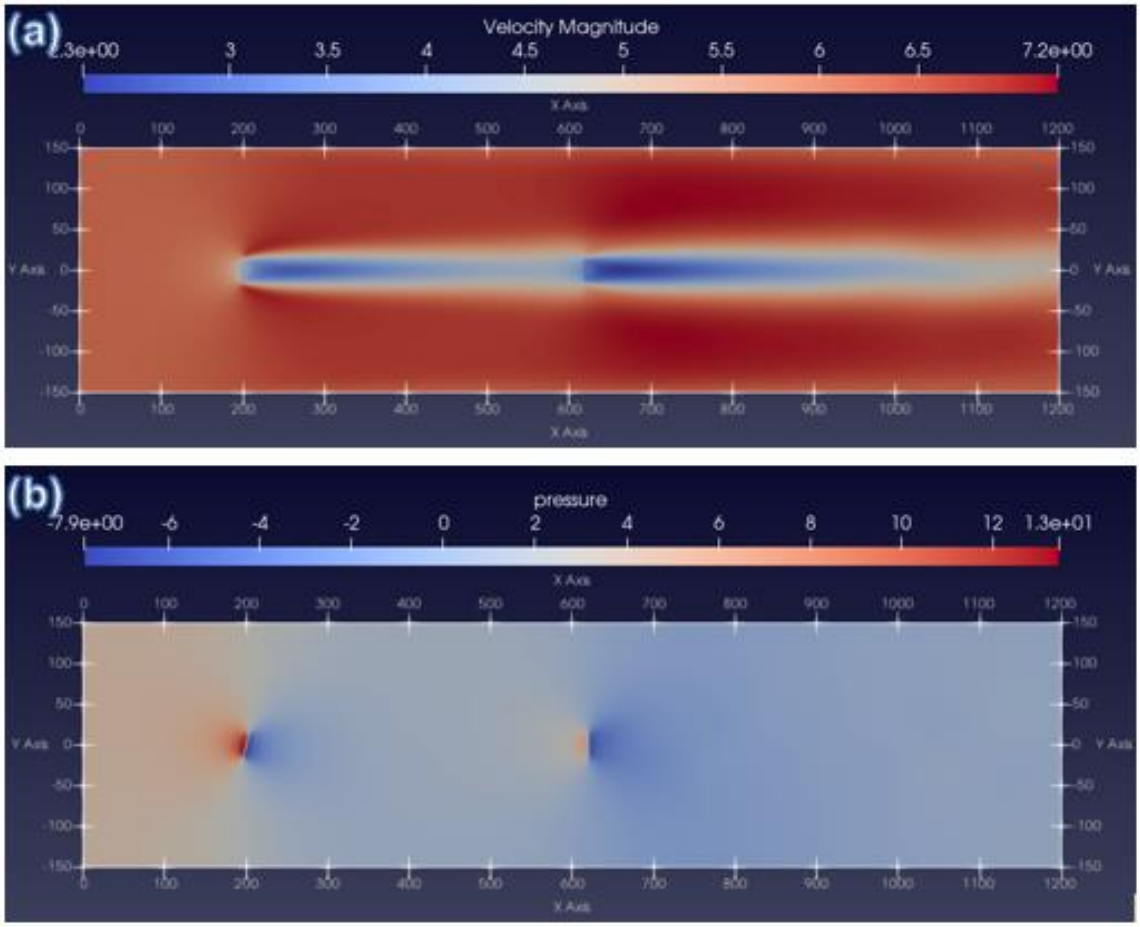

Figure 6-2. Aerodynamic profiles of a two-array turbine for a yaw angle of -5.78º of the upwind turbine (a) Instantaneous streamwise velocity field, $\boldsymbol{u_x}$; (b) Pressure profile.

On the other hand, three contiguous tests have also been carried out with 10 scenarios each where the downstream turbine angle is allowed to vary. In this way, it can be studied what would happen if a position control for the two turbines was performed.

Table 6-2. Optimization results for a mesh of [800x200] and angle variable for the downstream turbine.

Test	Average Power Output (W)	Yaw angle T1	Yaw angle T2
1	136,439.92	-7.92º	4.02º
2	134,529.78	-13.01º	-0.50º
3	137,014.94	-1.19º	9.30º

Although it is true that the values obtained for the three best cases of Table 6-2 are better than the values obtained for the case without variation of the downstream turbine angle, they are also subject to greater variability (differences of about 10% between the scenario with the highest average power output and the worst scenario, compared to 5% in the previous case). In addition, it is observed that the angles required to achieve a higher power output are larger than in the previous case. This is not what is desired, as small angles are sought that does not imply a large dynamic change in the operation of the wind turbine, as in the case of fluctuations in the wind direction, it is not desirable to be making large changes in the direction of the wind turbine at all times.

Interestingly, the best scenario in this batch of tests is one in which the angle of rotation of the first turbine is small while the angle of misalignment of the second turbine is high. This is something that has not been considered in this paper, which is the change in direction of the downstream turbines to avoid the wake of the upstream turbines. It is also observed that when one turbine rotates in one direction, the other turbine rotates in the opposite direction in order to avoid the wake to a greater extent.

Logically, the control of the yaw angle change of all the turbines in the wind farm requires a great effort that is not possible in many cases, and the control must be reduced to a few turbines, which would be those placed upstream. In this case, as there are only two turbines, simultaneous control of both turbines would be possible, but when the array is large enough, such instantaneous control would become more imprecise and slower.

6.2 Second mesh approach

For the second case with a mesh size of [1200x300], the same number of tests have been carried out with the same number of scenarios per test and therefore 30 scenarios in total. The best results obtained in each of the tests are shown in Table 6-3. Looking at the 30 scenarios in Appendix A.4, there are larger variations than for the [800x200] mesh, with variations of up to 10% between the best and worst average power output. Likewise, greater variability of the three yaw angles obtained is observed. However, a value very similar to those present in Table 6-1,

5.80º is obtained, which is not the best result of this batch but suggests that the best angle may be close to this value. The conclusion of these tests is that the greater the angle, the lower the energy production, however, taking into account the results of the previous section, it is possible that the optimum value is closer to 5.80º than the 1.65º that achieves the best result of these three.

Table 6-3. Optimization results for a mesh of [1200x300].

Test	Average Power Output (W)	Yaw angle
1	747,085.25	-5.80º
2	751,374.38	1.65º
3	735,876.63	-10.55º

For this mesh, the possibility of incorporating a downstream turbine swing has also been studied. Table 6-4 shows the best results obtained. As in the previous case, higher average power output is obtained than in the case where only the upstream wind turbine rotates.

The best result obtained is for the situation in which both wind turbines are out of alignment with the incident wind at a similar angle, close to 2°. This is a fairly small value in terms of angle but it can be fundamental for improving energy production given that 2% more power is produced than in the best case obtained with the upwind turbine rotating exclusively, almost just by rotating 2º the downstream turbine.

Table 6-4. Optimization results for a mesh of [1200x300] and angle variable for the downstream turbine.

Test	Average Power Output (W)	Yaw angle T1	Yaw angle T2
1	759,273.69	2.14º	1.02º
2	746,236.31	-6.21º	-10.65º
3	764,448.81	2.22º	2.36º

Finally, it should be added that within the thirty scenarios, the biggest difference between the best and the worst power result is 10%, as in the case of exclusive rotation of the upwind turbine.

6.3 Third mesh approach

For the third analysis with a mesh size of [1600x400], there are also 3 tests with 10 scenarios per test. As in the two previous cases, the three best results are presented below.

Table 6-5. Optimization results for a mesh of [1600x400].

Test	Average Power Output (W)	Yaw angle
1	2,541,808.00	0.91º
2	2,542,770.00	-2.59º
3	2,566,472.50	-1.76º

Unlike the previous cases, there is no scenario where a high yaw angle implies a good result. For this mesh, quite small angles, below 3º, are achieved. So far, all the best results for each mesh size have resulted in a small yaw angle (<6º), which indicates that in the absence of a study of the largest mesh size, small angles are the ideal result to improve the energy extraction of the wind farm.

6.4 Fourth mesh approach

For the fourth and last analysis with a mesh size of [2000x500], 3 tests with 10 scenarios per test are also carried out. Table 6-6 presents the best results that were obtained.

Table 6-6. Optimization results for a mesh of [2000x500].

Test	Average Power Output (W)	Yaw angle
1	9,082,889.00	1.23º
2	8,760,186.00	12.84º
3	8,727,708.00	-0.64º

Once again, the same behaviour is observed as in the previous cases, where the best result is presented for small yaw angles. In this case, an angle of 1.23º is the one that allows the greatest possible extraction of energy.

It is also worth noting how a high angle of misalignment has made it into the list of the top three scenarios. This, as in the previous cases, is due to the fact that at large angles, the wake deflection is so large that the second wind turbine

produces more energy. However, the extraction of the first wind turbine is reduced to such an extent that, in general, a higher extraction is achieved if the wind turbine is only slightly rotated.

6.5 Three turbine array study

In addition to the study of the optimisation of a two-turbine array, an analysis of three turbines aligned in the wind direction is carried out. Basically, this is an extension of the study carried out so far, where a new turbine is added. This new turbine is placed at 7D from the second turbine (14D with respect to the first turbine), which places the centre of its disk rotor at the point in the domain (1040,0). Logically, this turbine has the same disk rotor diameter of 60 m as the other two turbines.

The study consists of 6 tests with 10 scenarios per test, giving 60 scenarios in total for the 180 scenarios that have been carried out for the two-turbine array. These six tests are performed in pairs, i.e., the first two are for the case where only the upwind turbine is able to perform a turning motion; the second two are for the case where both the first and the second turbine are able to perform a turning motion; and finally, the last two tests allow for the turning motion of all three turbines.

Table 6-7 presents the best-case scenarios for each test performed for the three-turbine array. These 6 tests are performed for the simplest mesh size of [800x200] due to computational time constraints.

Table 6-7. Optimization results for a three-turbine array.

Test	Average Power Output (W)	Yaw angle T1	Yaw angle T2	Yaw angle T3
1	172,225.28	1.17º	0.00º	0.00º
2	170,928.52	-11.17º	0.00º	0.00º
3	170,111.06	14.77º	-12.69º	0.00º
4	171,644.50	6.96º	17.88º	0.00º
5	170,613.719	-12.86º	13.57º	5.89º
6	167,926.688	-5.77º	-6.07º	-16.37º

Of the six scenarios presented in Table 6-7, the best result is obtained for the case where only the first turbine is rotated. The second-best result is given for the scenario in which both the first and second turbines are rotated, but with yaw angles significantly higher than for the best available scenario. What is clear is that turning all three turbines gives the worst possible result and that the most downstream turbine should not be turned, which makes sense considering that turning a turbine is to prevent the downstream turbine from suffering the consequences of the wake of the upstream turbine. By being the last turbine, and not having any turbines downstream, it only reduces the total energy extraction.

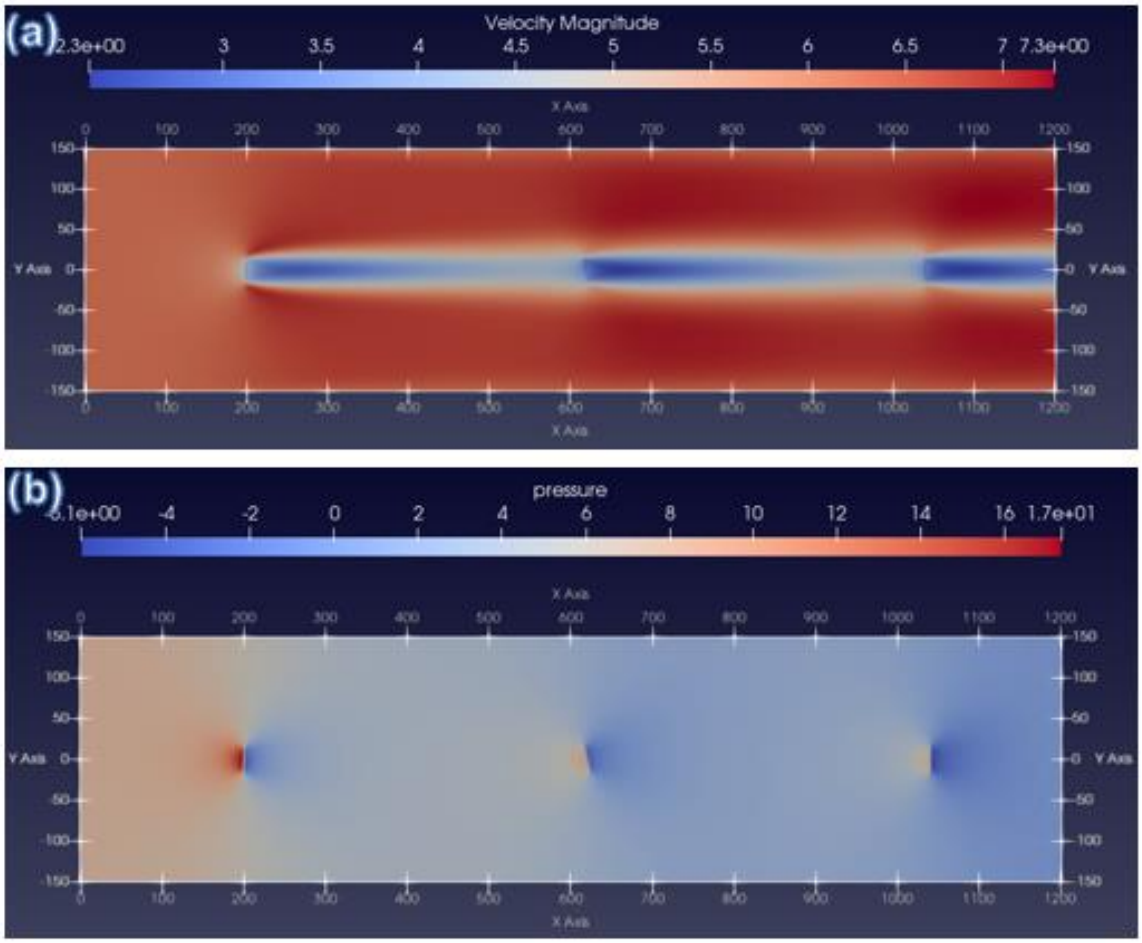

Figure 6-3. Aerodynamic profiles of a three-turbine array (a) Instantaneous streamwise velocity field, $\boldsymbol{u_x}$; (b) Pressure profile.

In Figure 6-3, the velocity and pressure profiles for the three-turbine array are shown, following the same logic as the profiles presented in Figure 6-2. In this example model, both the upstream turbine and the intermediate turbine are

inclined at a certain yaw angle. It can be seen that for each of the downstream turbines, there is an increasingly smaller wake for which the velocity is lower due to the wake generated by the upstream turbine. Likewise, higher overpressures are produced in the case of the upwind turbine.

7 CONCLUSION

This paper presents a novel model based on LES and uses the Actuator Disk Model to study the feasibility of improving the performance of a wind farm through wake steering. The validation of the model has been successful, achieving relative errors with respect to the benchmark model of less than 5% for simple meshes and reaching errors close to 1% for more complex meshes. Within the three different yaw angles analysed, results closer to the benchmark have been obtained for the 0º case, basically due to the fact that larger mesh sizes have been studied.

Comparing the three angles analysed for the meshes that all three have, a number of conclusions can be drawn. In order to achieve a lower error, the model requires a smaller number of elements for the 10º and 20º cases. Also, for the 0º case, velocity peaks have been observed at the periphery of the disk rotor, which, while they do occur in reality and are presented in the benchmark model, are too high in the model. This does not occur in the 10º and 20º models and is more in line with the benchmark. In addition, the adjustment of the *K_para* parameter in the sensitivity analysis has made it possible to reduce the error, especially for small distances to the downstream disk rotor. Since this parameter allows for regulating the flow through the rotor disk, for a distance of 2.5D the error is improved at the cost of an increase of the error in x = 5.5D and x = 8D. On the other hand, for short distances, it has also been observed that the velocity profile is thinner than the benchmark, but as the downstream distance increases, this effect dissipates and the validation is better adjusted. As for the wake deviation due to the yaw angle, the model perfectly matches the benchmark, thus achieving a wake deviation that is close to reality.

The execution of the sensitivity analysis has made it possible to establish a greater closeness between the results obtained by this model and those of Jiménez et al. (2009). This analysis has allowed establishing the meshes beyond which the error converges and it is not profitable to continue increasing the mesh size. Thus, it has been possible to know the limitations and virtues of the model

by establishing the mesh sizes that are computationally optimal in order not to waste computational time, which is very valuable in the field of CFD.

In terms of optimisation, different conclusions can be drawn from the three different analyses. In the case where only the first turbine is allowed to move, the best result obtained is close to 5º, thanks to which, for the smallest mesh of [800x200] and a *K_para* value of 1.9, an average power output of 134,947.16 N can be achieved. Bearing in mind that for this mesh, the power that would be extracted if both turbines were perpendicular to the incident wind would be 133,232.84 W. This implies that if the upwind turbine is rotated 5º, an increase of about 1.3% is achieved. This may not seem much, but for large turbines where the output is much larger than a few kW, this increase can be substantial. For the rest of the *K_para* values analysed, the best results offer values of the yaw angle of the first turbine even smaller than those 5º of the simple mesh. Values between 1 and 3º are the most common among the best results obtained. Implying that small turning angles are optimal for slightly deflecting the turbine wake and increasing the total extraction of the wind farm.

For the case where both turbines are allowed to rotate, no absolute conclusions can be drawn as there have been several cases where it would be optimal for both turbines to rotate at a small angle (<3º) while other scenarios have established small angles for the first turbine but relatively large angles for the second turbine (>9º). In the latter case, a power output (for the *K_para* case of 1.9) of 137,014.94 W is achieved, which is an increase over the no-turn case of 2.8%. This is an improvement over the case in which only the upstream turbine was rotating.

Finally, the last analysis of three turbines indicates that the best option when there is a long line of wind turbines is that the turbines that are closest to the incident wind are the ones that rotate. Meaning that not all of them have to rotate. In the case analysed, it has been observed that rotating the third wind turbine would be detrimental to obtaining more average power and that the best option is for only the first wind turbine to rotate.

In conclusion, the model is able to approximately predict the behaviour of the wake of a wind turbine in the presence of variations in the yaw angle of the wind turbine with respect to the incident wind. Furthermore, although not detailed in this paper, it is also able to predict the behaviour of the wake in the presence of variations in the direction of the incident wind. In addition, the Bayesian optimization performed allows knowing in a simple and fast way how a turbine system would behave under different angle arrangements and atmospheric conditions.

8 FURTHER WORK

Due to technical time constraints, it has not been possible to perform either a 3D validation of the model or a 3D Bayesian optimization. Therefore, it has not been possible to study the behaviour of the wake under rotation. That is to say, only the ADM-NR has been studied and not the ADM-R. Therefore, in a future analysis of this model, it is expected to be able to validate the model in 3D and carry out a Bayesian optimization of it.

As for the validation, due to lack of time, the validation of a yaw angle of 30º present in Jiménez et al. (2009) has not been carried out, which meant that the Bayesian optimisation for values between -30º and 30º was not performed. In the future, in order to revalidate the model, should be studied the wake generated in the presence of greater variability of angles and the face of different benchmark problems.

On the other hand, the optimization has only been performed for a two and three-turbine array, not for a wind farm with several rows and columns upstream. Therefore, the possible influence of neighbouring turbines rotating in the wake of adjacent turbines has not been studied. In addition, Bayesian optimisation benefits from the number of scenarios analysed. The more scenarios analysed, the more optimal the final result is. In this paper, a total of 240 scenarios have been analysed, which would be insufficient for more precise results.

REFERENCES

[1] M. Allen *et al.*, “Summary for Policymakers. In: Global Warming of 1.5°C. An IPCC Special Report on the impacts of global warming of 1.5°C above pre-industrial levels and related global greenhouse gas emission pathways, in the context of strengthening the global response to the threat of climate change, sustainable development, and efforts to eradicate poverty,” 2018.

[2] United Nations: Framework Convention on Climate Change, “Adoption of the Paris Agreement,” 2015.

[3] R. J. Barthelmie *et al.*, “Modelling and measuring flow and wind turbine wakes in large wind farms offshore,” *Wind Energy*, vol. 12, no. 5, pp. 431–444, Jul. 2009, doi: 10.1002/WE.348.

[4] K. S. Hansen, R. J. Barthelmie, L. E. Jensen, and A. Sommer, “The impact of turbulence intensity and atmospheric stability on power deficits due to wind turbine wakes at Horns Rev wind farm,” *Wind Energy*, vol. 15, no. 1, pp. 183–196, Jan. 2012, doi: 10.1002/WE.512.

[5] R. J. Barthelmie *et al.*, “Modelling and measurements of wakes in large wind farms,” *JPhCS*, vol. 75, no. 1, p. 012049, Jun. 2007, doi: 10.1088/1742-6596/75/1/012049.

[6] J. Meyers and C. Meneveau, “Optimal turbine spacing in fully developed wind farm boundary layers,” 2011, doi: 10.1002/we.469.

[7] G. Marmidis, S. Lazarou, and E. Pyrgioti, “Optimal placement of wind turbines in a wind park using Monte Carlo simulation,” *Renew Energy*, vol. 33, no. 7, pp. 1455–1460, Jul. 2008, doi: 10.1016/J.RENENE.2007.09.004.

[8] R. J. A. M. Stevens, D. F. Gayme, and C. Meneveau, “Effects of turbine spacing on the power output of extended wind-farms,” *Wind Energy*, vol. 19, no. 2, pp. 359–370, Feb. 2016, doi: 10.1002/WE.1835.

[9] R. J. A. M. Stevens, B. F. Hobbs, A. Ramos, and C. Meneveau, “Combining economic and fluid dynamic models to determine the optimal spacing in

very large wind farms," *Wind Energy*, vol. 20, no. 3, pp. 465–477, Mar. 2017, doi: 10.1002/WE.2016.

[10] Á. Jiménez, A. Crespo, and E. Migoya, "Application of a LES technique to characterize the wake deflection of a wind turbine in yaw," 2009.

[11] E. Son, S. Lee, B. Hwang, and S. Lee, "Characteristics of turbine spacing in a wind farm using an optimal design process," *Renew Energy*, vol. 65, pp. 245–249, May 2014, doi: 10.1016/J.RENENE.2013.09.022.

[12] M. C. Brower and N. M. Robinson, "THE OPENWIND DEEP-ARRAY WAKE MODEL Development and Validation Chief Technical Officer," 2012.

[13] B. Sanderse, S. P. van der Pijl, and B. Koren, "Review of computational fluid dynamics for wind turbine wake aerodynamics," *Wind Energy*, vol. 14, no. 7, pp. 799–819, Oct. 2011, doi: 10.1002/WE.458.

[14] A. Jimenez, A. Crespo, E. Migoya, and J. Garcia, "Large-eddy simulation of spectral coherence in a wind turbine wake," *Environmental Research Letters*, vol. 3, no. 1, p. 015004, Jan. 2008, doi: 10.1088/1748-9326/3/1/015004.

[15] A. el Kasmi and C. Masson, "An extended k–ε model for turbulent flow through horizontal-axis wind turbines," *Journal of Wind Engineering and Industrial Aerodynamics*, vol. 96, no. 1, pp. 103–122, Jan. 2008, doi: 10.1016/J.JWEIA.2007.03.007.

[16] S. Ivanell, J. N. Sørensen, R. Mikkelsen, and D. Henningson, "Analysis of numerically generated wake structures," *Wind Energy*, vol. 12, no. 1, pp. 63–80, Jan. 2009, doi: 10.1002/WE.285.

[17] J. N. Sùrensen, W. Z. Shen, and X. Munduate, "Analysis of Wake States by a Full-®eld Actuator Disc Model," 2018, doi: 10.1002/(SICI)1099-1824(199812)1:2.

[18] J. N. Sørensen and C. W. Kock, “A model for unsteady rotor aerodynamics,” *Journal of Wind Engineering and Industrial Aerodynamics*, vol. 58, no. 3, pp. 259–275, Dec. 1995, doi: 10.1016/0167-6105(95)00027-5.

[19] J. Annoni, P. M. O. Gebraad, A. K. Scholbrock, P. A. Fleming, and J. W. van Wingerden, “Analysis of axial-induction-based wind plant control using an engineering and a high-order wind plant model,” *Wind Energy*, vol. 19, no. 6, pp. 1135–1150, Jun. 2016, doi: 10.1002/WE.1891.

[20] F. Port, C. Meneveau, and M. B. Parlange, “A scale-dependent dynamic model for large-eddy simulation: application to a neutral atmospheric boundary layer,” *J. Fluid Mech*, vol. 415, pp. 261–284, 2000, doi: 10.1017/S0022112000008776.

[21] M. Chamecki, C. Meneveau, and M. B. Parlange, “Large eddy simulation of pollen transport in the atmospheric boundary layer,” *J Aerosol Sci*, vol. 40, no. 3, pp. 241–255, Mar. 2009, doi: 10.1016/J.JAEROSCI.2008.11.004.

[22] J. P. Goit and J. Meyers, “Optimal control of wind farm power extraction in large eddy simulations,” *32nd ASME Wind Energy Symposium*, 2014, doi: 10.2514/6.2014-0709.

[23] L. Vollmer, G. Steinfeld, D. Heinemann, and M. Kühn, “Estimating the ake deflection donstream of a ind turbine in different atmospheric stabilities: An les study,” *Wind Energy Science*, vol. 1, no. 2, pp. 129–141, Jul. 2016, doi: 10.5194/WES-1-129-2016.

[24] P. M. O. Gebraad *et al.*, “Wind plant power optimization through yaw control using a parametric model for wake effects—a CFD simulation study,” *Wind Energy*, vol. 19, no. 1, pp. 95–114, Jan. 2016, doi: 10.1002/WE.1822.

[25] F. Porté-Agel and Y.-T. Wu, “Large-Eddy Simulation of Wind-Turbine Wakes: Evaluation of Turbine Parametrisations,” 2010.

[26] M. Calaf, C. Meneveau, and J. Meyers, “Large eddy simulation study of fully developed wind-turbine array boundary layers,” *Physics of Fluids*, vol. 22, no. 1, p. 015110, Jan. 2010, doi: 10.1063/1.3291077.

[27] F. Porté-Agel and Y.-T. Wu, “Simulation of Turbulent Flow Inside and Above Wind Farms: Model Validation and Layout Effects,” 2012.

[28] J. P. Goit and J. Meyers, “Optimal control of energy extraction in wind-farm boundary layers,” *J Fluid Mech*, vol. 768, pp. 5–50, 2015, doi: 10.1017/JFM.2015.70.

[29] R. J. A. M. Stevens, L. A. Martínez-Tossas, and C. Meneveau, “Comparison of wind farm large eddy simulations using actuator disk and actuator line models with wind tunnel experiments,” 2017.

[30] J. Schottler, A. Hölling, J. Peinke, and M. Hölling, “Wind tunnel tests on controllable model wind turbines in yaw”, doi: 10.2514/6.2016-1523.

[31] F. Campagnolo, V. Petrović, C. L. Bottasso, and A. Croce, “Wind tunnel testing of wake control strategies,” *Proceedings of the American Control Conference*, vol. 2016-July, pp. 513–518, Jul. 2016, doi: 10.1109/ACC.2016.7524965.

[32] J. Quick, J. Annoni, R. King, K. Dykes, P. Fleming, and A. Ning, “Optimization under Uncertainty for Wake Steering Strategies,” *J Phys Conf Ser*, vol. 854, no. 1, Jun. 2017, doi: 10.1088/1742-6596/854/1/012036.

[33] A. Rott, B. Doekemeijer, J. Kristina Seifert, J. W. van Wingerden, and M. Kühn, “Robust active wake control in consideration of wind direction variability and uncertainty,” *Wind Energy Science*, vol. 3, no. 2, pp. 869–882, 2018, doi: 10.5194/WES-3-869-2018.

[34] K. A. Kragh, M. H. Hansen, C. A. Knud Kragh, K. A. Kragh, and M. H. Hansen, “Load alleviation of wind turbines by yaw misalignment,” *Wind Energy*, vol. 17, no. 7, pp. 971–982, Jul. 2014, doi: 10.1002/WE.1612.

[35] D. Medici and P. H. Alfredsson, “Measurements on a wind turbine wake: 3D effects and bluff body vortex shedding,” *Wind Energy*, vol. 9, no. 3, pp. 219–236, May 2006, doi: 10.1002/WE.156.

[36] P. M. O. Gebraad and J. W. van Wingerden, “Maximum power-point tracking control for wind farms,” *Wind Energy*, vol. 18, no. 3, pp. 429–447, Mar. 2015, doi: 10.1002/WE.1706.

[37] K. Johnson and G. Fritsch, “Assessment of extremum seeking control for wind farm energy production,” *Wind Engineering*, vol. 36, no. 6, pp. 701–716, Dec. 2012, doi: 10.1260/0309-524X.36.6.701.

[38] T. Horvat, V. S. Spudi´c, and M. Baoti´cbaoti´c, “Quasi-stationary optimal control for wind farm with closely spaced turbines,” 2011.

[39] M. Becker *et al.*, “Improved modelling of wake aerodynamics and assessment of new farm control strategies,” *J Phys Conf Ser*, vol. 75, no. 1, p. 012039, Jul. 2007, doi: 10.1088/1742-6596/75/1/012039.

[40] M. Soleimanzadeh, R. Wisniewski, and K. Johnson, “A distributed optimization framework for wind farms,” *Journal of Wind Engineering & Industrial Aerodynamics*, vol. 123, pp. 88–98, Dec. 2013, doi: 10.1016/J.JWEIA.2013.08.011.

[41] J. Bartl and L. Saetran, “Experimental testing of axial induction based control strategies for wake control and wind farm optimization,” 2016, doi: 10.1088/1742-6596/753/3/032035.

[42] M. Coquelet, M. Moens, L. Bricteux, J.-B. Crismer, and P. Chatelain, “Performance assessment of wake mitigation strategies,” 2022, doi: 10.1088/1742-6596/2265/3/032078.

[43] J. Park, S. D. Kwon, and K. Law, “A Data-Driven, Cooperative Approach for Wind Farm Control: A Wind Tunnel Experimentation,” *Energies 2017, Vol. 10, Page 852*, vol. 10, no. 7, p. 852, Jun. 2017, doi: 10.3390/EN10070852.

[44] J. Park and K. H. Law, “Cooperative wind turbine control for maximizing wind farm power using sequential convex programming,” *Energy Convers Manag*, vol. 101, pp. 295–316, Sep. 2015, doi: 10.1016/J.ENCONMAN.2015.05.031.

[45] Fernando Nogueira, “{Bayesian Optimization}: Open source constrained global optimization tool for {Python}.” 2014. Accessed: Jun. 12, 2022. [Online]. Available: https://github.com/fmfn/BayesianOptimization

[46] K. Jinkyoo Park, K. H. Law, and J. Park, “A Bayesian optimization approach for wind farm power maximization,” *https://doi.org/10.1117/12.2084184*, vol. 9436, pp. 46–57, Mar. 2015, doi: 10.1117/12.2084184.

[47] D. Medici and J. A. Dahlberg, “Potential improvement of wind turbine array efficiency by active wake control (AWC),” 2003. https://www.diva-portal.org/smash/record.jsf?pid=diva2%3A14557&dswid=5414 (accessed Jun. 12, 2022).

[48] J. Mockus, T. Vytautas, and Z. Antanas, “Toward global optimization, volume 2, chapter bayesian methods for seeking the extremum,” 1978. https://scholar.google.com/scholar_lookup?title=Towards+global+optimization&author=J.+Mockus&author=A.+Fretitas&author=J.+A.+Castelanous&publication_year=1978 (accessed Jun. 12, 2022).

APPENDICES

A.1 2D VALIDATION FOR A YAW ANGLE OF 0º

Table 8-1. Error breakdown for a 0º case scenario.

Mesh	K_para	ε(2.5D)	ε(5.5D)	ε(8D)	ε_{avg}
[800x200]	0.5	37.33%	4.16%	2.02%	14.50%
[800x200]	0.8	17.11%	4.86%	8.18%	10.05%
[800x200]	0.9	11.66%	7.22%	9.76%	9.55%
[800x200]	1	6.70%	9.35%	11.18%	9.07%
[800x200]	1.05	4.37%	10.34%	11.83%	8.85%
[800x200]	1.1	2.14%	11.29%	12.45%	8.63%
[1200x300]	1	25.16%	0.43%	4.71%	10.10%
[1200x300]	1.1	20.91%	2.24%	5.90%	9.68%
[1200x300]	1.5	6.50%	8.20%	9.76%	8.15%
[1200x300]	1.6	3.42%	9.44%	10.55%	7.81%
[1200x300]	1.7	0.51%	10.60%	11.28%	7.47%
[1200x300]	1.8	2.24%	11.69%	11.96%	8.63%
[1600x400]	1	37.66%	5.60%	0.28%	14.52%
[1600x400]	1.8	11.97%	4.93%	7.04%	7.98%
[1600x400]	2	7.01%	6.85%	8.22%	7.36%
[1600x400]	2.2	2.49%	8.59%	9.28%	6.79%
[1600x400]	2.3	0.38%	9.38%	9.76%	6.51%
[1600x400]	2.4	1.66%	10.14%	10.22%	7.34%
[2000x500]	1	46.67%	9.97%	2.93%	19.86%
[2000x500]	2.2	13.88%	3.17%	5.31%	7.46%
[2000x500]	2.4	9.87%	4.68%	6.21%	6.92%
[2000x500]	2.8	2.70%	7.30%	7.73%	5.91%
[2000x500]	3	0.53%	8.45%	8.39%	5.79%
[2000x500]	3.1	2.08%	8.99%	8.69%	6.58%
[2000x500]	3.2	3.57%	9.50%	8.98%	7.35%
[2400x600]	1	53.41%	13.25%	5.37%	24.01%
[2400x600]	3	9.11%	3.86%	4.97%	5.98%

[2400x600]	3.4	3.39%	5.83%	6.05%	5.09%
[2400x600]	3.8	1.74%	7.53%	6.95%	5.41%
[2400x600]	3.5	2.05%	6.28%	6.29%	4.87%
[2400x600]	3.6	0.75%	6.71%	6.52%	4.66%
[2800x700]	3.8	6.69%	3.47%	3.93%	4.70%
[2800x700]	4	4.39%	4.21%	4.29%	4.30%
[2800x700]	4.2	2.21%	4.89%	4.63%	3.91%
[2800x700]	4.4	0.12%	5.54%	4.94%	3.53%
[2800x700]	4.5	0.88%	5.84%	5.09%	3.94%
[2800x700]	4.6	1.87%	6.14%	5.23%	4.41%
[3200x800]	4.8	3.73%	3.08%	2.74%	3.18%
[3200x800]	5	1.95%	3.59%	2.96%	2.83%
[3200x800]	5.2	0.24%	4.07%	3.17%	2.49%
[3200x800]	5.4	1.39%	4.52%	3.35%	3.09%
[3600x900]	5.6	3.75%	1.67%	1.02%	2.15%
[3600x900]	5.8	2.27%	2.05%	1.16%	1.83%
[3600x900]	6	0.84%	2.41%	1.29%	1.52%
[3600x900]	6.2	0.53%	2.76%	1.41%	1.57%

A.2 2D VALIDATION FOR A YAW ANGLE OF 10º

Table 8-2. Error breakdown for a 10º case scenario.

Mesh	K_para	ε(2.5D)	ε(5.5D)	ε(8D)	ε_{avg}
[800x200]	1.5	24.56%	0.16%	5.04%	9.92%
[800x200]	1.8	17.59%	2.71%	6.78%	9.03%
[800x200]	2.2	9.81%	5.81%	8.62%	8.08%
[800x200]	2.5	4.83%	7.74%	9.73%	7.43%
[800x200]	2.8	0.43%	9.41%	10.67%	6.83%
[1200x300]	2.5	22.14%	1.49%	2.69%	8.77%
[1200x300]	3	15.29%	0.96%	3.96%	6.73%
[1200x300]	3.5	9.48%	2.94%	4.94%	5.79%
[1200x300]	3.8	6.39%	3.97%	5.42%	5.26%
[1200x300]	4.2	2.66%	5.18%	5.97%	4.60%
[1600x400]	3.5	22.63%	4.24%	0.66%	9.18%
[1600x400]	4	17.85%	2.79%	0.08%	6.91%
[1600x400]	4.5	13.64%	1.59%	0.37%	5.20%
[1600x400]	5	9.90%	0.58%	0.71%	3.73%
[1600x400]	5.5	6.56%	0.28%	0.96%	2.60%
[2000x500]	4	28.17%	8.56%	4.66%	13.80%
[2000x500]	5	20.58%	6.68%	4.16%	10.47%
[2000x500]	6	14.46%	5.35%	3.94%	7.92%
[2000x500]	6.5	11.82%	4.84%	3.90%	6.85%
[2000x500]	7	1.66%	2.16%	1.35%	1.72%

A.3 2D VALIDATION FOR A YAW ANGLE OF 20º

Table 8-3. Error breakdown for a 20º case scenario.

Mesh	**K_para**	**ε(2.5D)**	**ε(5.5D)**	**ε(8D)**	**ε_{avg}**
[800x200]	1.5	11.42%	3.44%	7.30%	7.39%
[800x200]	1.6	9.12%	4.51%	8.00%	7.21%
[800x200]	1.8	4.87%	6.46%	9.26%	6.86%
[800x200]	1.9	2.91%	7.35%	9.83%	6.70%
[800x200]	2	1.04%	8.19%	10.37%	6.53%
[1200x300]	2	16.16%	0.14%	4.08%	6.80%
[1200x300]	2.2	12.87%	1.31%	4.98%	6.39%
[1200x300]	2.4	9.83%	2.63%	5.79%	6.08%
[1200x300]	2.8	4.35%	4.95%	7.18%	5.49%
[1200x300]	3	1.88%	5.99%	7.78%	5.21%
[1600x400]	3	13.00%	0.27%	2.97%	5.41%
[1600x400]	3.2	10.78%	0.61%	3.46%	4.95%
[1600x400]	3.4	8.67%	1.44%	3.90%	4.67%
[1600x400]	3.8	4.77%	2.93%	4.69%	4.13%
[1600x400]	4	2.97%	3.60%	5.04%	3.87%
[2000x500]	4	11.94%	1.52%	1.02%	4.83%
[2000x500]	5	4.37%	1.06%	2.18%	2.54%
[2000x500]	5.5	1.14%	2.09%	2.59%	1.94%
[2000x500]	5.8	0.66%	2.63%	2.80%	2.03%
[2000x500]	6	1.80%	2.97%	2.91%	2.56%

A.4 OPTIMIZATION BREAKDOWN

Table 8-4. Optimization breakdown of [800x200] mesh.

Scenario	Test 1, P [W]	Test 2, P [W]	Test 3, P [W]
1	132,959.10	130,407.91	133,230.48
2	134,947.16	130,791.51	134,300.38
3	132,246.98	133,135.63	129,554.00
4	133,025.44	132,648.30	133,435.84
5	132,696.00	128,453.41	131,446.73
6	128,365.94	128,735.00	128,950.66
7	133,801.23	130,404.01	128,032.40
8	132,849.31	128,168.98	132,421.16
9	134,007.16	130,359.48	127,154.62
10	134,001.60	133,438.67	131,875.83
Best	134,947.16	133,438.67	134,300.38

Table 8-5. Optimization breakdown of [800x200] mesh and angle variable for the downstream turbine.

Scenario	Test 1, P [W]	Test 2, P [W]	Test 3, P [W]
1	136,439.92	134,529.78	137,014.94
2	131,160.95	133,492.13	130,457.27
3	132,129.06	131,307.48	128,756.33
4	133,711.53	126,486.45	131,723.63
5	126,649.89	130,798.17	129,555.72
6	130,907.59	128,877.98	123,588.02
7	130,894.61	127,467.94	129,790.70
8	131,351.12	123,881.58	125,358.64
9	130,168.73	133,681.11	130,751.22
10	130,318.14	130,604.91	129,738.42
Best	136,439.92	134,529.78	137,014.94

Table 8-6. Optimization breakdown of [1200x300] mesh.

Scenario	Test 1, P [W]	Test 2, P [W]	Test 3, P [W]
1	747,085.25	751,374.38	735,876.63
2	683,078.56	713,301.56	714,271.69
3	717,290.00	726,993.88	711,935.88
4	717,463.75	699,377.38	721,238.63
5	680,069.31	676,136.00	721,423.00
6	724,791.13	701,512.31	678,457.63
7	722,074.00	719,744.44	691,321.81
8	722,924.00	703,476.75	712,915.75
9	693,616.00	702,213.56	699,955.69
10	719,121.75	714,941.94	672,749.25
Best	747,085.25	751,374.38	735,876.62

Table 8-7. Optimization breakdown of [1200x300] mesh and angle variable for the downstream turbine.

Scenario	Test 1, P [W]	Test 2, P [W]	Test 3, P [W]
1	714,375.38	686,281.19	668,633.00
2	754,500.94	744,428.00	764,448.81
3	750,621.88	716,410.25	710,861.06
4	741,036.88	700934.75	722,703.19
5	730,518.31	708,152.00	751,313.63
6	721,862.13	710,850.88	703,076.81
7	741,687.88	730,086.69	727,550.75
8	755,740.00	705,531.00	751,949.75
9	759,273.69	723,575.13	731,827.75
10	724,696.50	746,236.31	707,041.06
Best	759,273.69	746,236.31	764,448.81

Table 8-8. Optimization breakdown of [1600x400] mesh.

Scenario	Test 1, P [W]	Test 2, P [W]	Test 3, P [W]
1	2,325,680.00	2,363,125.50	2,325,566.00
2	2,468,696.75	2,415,408.50	2,566,472.50
3	2,502,836.75	2,395,372.00	2,451,489.25
4	2,462,793.00	2,466,241.25	2,549,643.00
5	2,541,808.00	2,457,488.00	2,540,235.25
6	2,499,283.00	2,542,770.00	2,542,409.25
7	2,538,365.25	2,422,215.25	2,538,492.50
8	2,507,295.50	2,395,499.50	2,492,299.50
9	2,508,713.75	2,472,295.00	2,537,505.75
10	2,407,542.25	2,541,232.25	2,519,666.25
Best	2,541,808.00	2,542,770.00	2,566,472.50

Table 8-9. Optimization breakdown of [2000x500] mesh.

Scenario	Test 1, P [W]	Test 2, P [W]	Test 3, P [W]
1	8,361,882.00	8,207,991.00	8,611,836.00
2	9,082,889.00	8,760,186.00	8,333,003.00
3	8,328,631.00	8,578,217.00	8,554,435.00
4	8,371,684.00	8,573,438.00	8,572,644.00
5	8,092,237.00	8,007,542.00	8,727,708.00
6	8,629,750.00	8,663,339.00	8,090,575.00
7	8,501,154.00	8,690,532.00	8,676,048.00
8	8,414,299.00	8,575,160.00	8,538,962.00
9	8,682,150.00	8,683,656.00	7,923,936.00
10	8,366,309.00	8,466,559.00	7,898,988.00
Best	9,082,889.00	8,760,186.00	8,727,708.00

Table 8-10. Optimization breakdown of three-turbine array study.

Scenario	Test 1, P [W]	Test 2, P [W]	Test 3, P [W]	Test 4, P [W]	Test 5, P [W]	Test 6, P [W]
1	172,225.28	170,928.52	170,111.06	171,644.50	170,613.72	167,926.69
2	157,747.47	156,195.30	156,951.86	159,802.50	155,385.09	145,946.95
3	159,437.22	163,730.11	162,762.17	163,493.19	152,897.20	165,965.95
4	160,601.97	161,794.88	159,053.28	159,111.44	160,135.05	147,667.67
5	162,570.50	162,229.70	162,570.11	162,256.97	158,292.34	143,140.33
6	159,946.44	162,266.75	162,184.11	162,285.41	160,097.44	152,946.77
7	159,197.56	160,960.11	162,303.47	162,259.66	155,448.81	161,735.16
8	161,485.73	161,072.61	158,634.22	160,320.22	159,526.64	152,415.92
9	161,370.84	162,272.60	162,391.28	161,995.84	148,692.42	159,795.91
10	160,946.31	159,168.92	161,979.84	162,323.34	143,846.50	137,421.55
Best	172,225.28	170,928.52	170,111.06	171,644.50	170,613.72	167,926.69